Convective Transport of Peroxides by Thunderstorms Observed over the Central U.S. during DC3

M. C. Barth[1], M. M. Bela[2,3], A. Fried[4], P. O. Wennberg[5], J. D. Crounse[5], J. M. St. Clair[6], N. J. Blake[7], D. R. Blake[7], C. R. Homeyer[8], W. H. Brune[9], L. Zhang[9], J. Mao[10,11], X. Ren[12], T. B. Ryerson[13], I. B. Pollack[14], J. Peischl[13,15], R. C. Cohen[16], B. A. Nault[16], L. G. Huey[17], X. Liu[17] and C. A. Cantrell[2]

[1]Atmospheric Chemistry Observations and Modeling Laboratory and Mesoscale and Microscale Meteorology Laboratory, National Center for Atmospheric Research, Boulder, Colorado, USA

[2]Department of Atmospheric and Oceanic Sciences, University of Colorado, Boulder, Colorado, USA

[3]Laboratory for Atmospheric and Space Physics, University of Colorado, Boulder, Colorado, USA

[4]Institute for Arctic and Alpine Research, University of Colorado, Boulder, CO, USA

[5]California Institute of Technology, Pasadena, California, USA

[6]Joint Center for Earth Systems Technology, University of Maryland – Baltimore County / NASA-Goddard Space Flight Center, Greenbelt, Maryland

[7]Department of Chemistry, University of California, Irvine, California, USA

[8]School of Meteorology, University of Oklahoma, Norman, Oklahoma, USA

[9]Pennsylvania State University, University Park, Pennsylvania, USA

[10]Program in Atmospheric and Oceanic Sciences, Princeton University, Princeton, NJ, USA

[11]Geophysical Fluid Dynamics Laboratory, NOAA, Princeton, NJ, USA

[12]NOAA-Air Resources Laboratory, College Park, Maryland, USA

[13]Chemical Sciences Division, Earth System Research Laboratory, National Oceanic and Atmospheric Administration, Boulder, Colorado, USA

[14]Atmospheric Sciences Department, Colorado State University, Fort Collins, CO, USA

[15]Cooperative Institute for Research in Environmental Sciences, University of Colorado, Boulder, Colorado, USA

[16]University of California – Berkeley, Berkeley, California, USA

[17]Georgia Institute of Technology, Atlanta, GA, USA

34

35

36

37   Correspondence to: M. C. Barth (barthm@ucar.edu), Atmospheric Chemistry Observations and

38   Modeling Laboratory, National Center for Atmospheric Research, 3450 Mitchell Lane, Boulder,

39   Colorado, USA

40

41   **Key Points:**
42   1. Peroxide scavenging efficiencies derived from measurements
43   2. Hydrogen peroxide is readily removed by storms
44   3. Methyl hydrogen peroxide scavenging correlated with ice, entrainment and lightning-NOx

2

Abstract

One of the objectives of the Deep Convective Clouds and Chemistry (DC3) field experiment was to determine the scavenging of soluble trace gases by thunderstorms. We present an analysis of scavenging of hydrogen peroxide (H_2O_2) and methyl hydrogen peroxide (CH_3OOH) from six DC3 cases that occurred in Oklahoma and northeast Colorado. Estimates of H_2O_2 scavenging efficiencies are comparable to previous studies ranging from 79-97% with uncertainties of 5-23%. CH_3OOH scavenging efficiencies ranged from 12-84% with uncertainties of 15-67%. The wide range of CH_3OOH scavenging efficiencies is surprising, as previous studies suggested that CH_3OOH scavenging efficiencies would be <10%. Cloud chemistry model simulations of one DC3 storm produced CH_3OOH scavenging efficiencies of 26-61% depending on the ice retention factor of CH_3OOH during cloud drop freezing, suggesting ice physics impacts CH_3OOH scavenging. The highest CH_3OOH scavenging efficiencies occurred in two severe thunderstorms, but there is no obvious correlation between the CH_3OOH scavenging efficiency and the storm thermodynamic environment. We found a moderate correlation between the estimated entrainment rates and CH_3OOH scavenging efficiencies. The production of nitric oxide from lightning may influence CH_3OOH convective outflow mixing ratios by reducing CH_3OOH production because methyl peroxy radical reacts with nitric oxides instead of hydroperoxy radical. However, parcel model simulations with added nitric oxide do not differ from those without a nitric oxide source. To determine why CH_3OOH can be substantially removed from storms, future studies should examine effects of entrainment rate, retention of CH_3OOH in frozen cloud particles during drop freezing, and lightning-NO_x production.

1. Introduction

To understand the radiative impact of ozone in the upper troposphere (UT), ozone chemical sources in the UT must be quantified. Ozone (O_3) is produced by the reactions between peroxy radicals (e.g. hydroperoxy and methyl hydroperoxy radicals, HO_2 and CH_3OO, respectively) and nitric oxide (NO) to form nitrogen dioxide (NO_2), which subsequently photodissociates to form O_3. Thus, odd hydrogen ($HO_x = OH + HO_2$; OH is hydroxyl radical) and nitrogen oxides ($NO_x = NO + NO_2$) are key precursors to O_3. Although the primary formation of HO_x radicals is from O_3 photodissociation, oxidation of volatile organic compounds (VOCs), as well as their photodissociation, is also important. A source of these VOCs and NO_x in the UT is in convective outflow regions, where VOCs are transported from the boundary layer (BL) to the UT and NO_x is formed from lightning. However, many key HO_x precursors, including formaldehyde (CH_2O), hydrogen peroxide (H_2O_2), and methyl hydrogen peroxide (CH_3OOH), are soluble and can be partially removed from the atmosphere via dissolution into cloud drops that grow into rain, snow, graupel, and hail precipitating to the ground. Quantifying the fraction of HO_x precursors that are scavenged (or conversely transported to the UT) improves the estimation of O_3 production in convective outflow regions. In this paper, we determine the scavenging efficiencies (SE) of H_2O_2 and CH_3OOH based on aircraft measurements obtained during the Deep Convective Cloud and Chemistry (DC3) field experiment [Barth et al., 2015]. Fried et al. [2015] perform a similar analysis for CH_2O while Bela et al. [2015] evaluate the convective transport of nitric acid, H_2O_2, CH_2O, sulfur dioxide, and CH_3OOH in a 3-dimensional cloud chemistry model with observations, and calculate the fraction of these species removed for four DC3 thunderstorm cases.

4

90   Previous studies suggest convective transport of HO_x precursors play an important role in

91   controlling O_3 mixing ratios in the UT. Measurements of UT HO_x during the NASA STRAT

92   (1996) campaign occasionally exceeded theoretical estimates of HO_x concentrations, suggesting

93   an additional source of UT HO_x that was proposed to be convective transport of CH_2O, H_2O_2,

94   and CH_3OOH [Jaegle et al., 1997; Prather and Jacob, 1997; Wennberg et al., 1998].

95   Measurements from the NASA PEM-Tropics (1999) campaign revealed an enhancement of

96   CH_3OOH and a lack of enhancement of H_2O_2 in aged convective outflow over the tropical

97   Pacific, supporting the importance of convective transport for sources of hydrogen oxide radicals

98   in the upper troposphere [Ravetta et al., 2001]. Cohan et al [1999] estimated that H_2O_2 had 55-

99   70% scavenging efficiency based on measurements of tropical oceanic convection, while

100   CH_3OOH showed no apparent scavenging. Peroxide measurements from the INTEX-A field

101   campaign revealed that H_2O_2 was depleted while CH_3OOH was enhanced in convective outflow

102   regions compared to the background UT [Snow et al., 2007]. These prior measurements in

103   STRAT, PEM Tropics-B, and INTEX-A did not gather simultaneous inflow and outflow trace

104   gas measurements of convection to allow for estimates of peroxide scavenging. An

105   intercomparison study of cloud-scale chemistry models [Barth et al., 2007b] showed a large

106   variation in predictions of CH_2O and H_2O_2 that depended on whether or not the trace gas was

107   retained in frozen particles (snow, graupel or hail).

108

109   Other previous studies have indicated an unexpected reduced amount of CH_3OOH in the marine

110   boundary layer impacted by clouds compared to the reduction that would be expected due to gas-

111   phase photochemistry. Fried et al. [2003] discuss conditions at very low NO mixing ratios (< 5

112   pptv) where box model calculations predicted CH_3OOH mixing ratios to be 2-3 times greater

113   than nearby CH_3OOH observations. While we expect CH_3OOH to be higher at low NO mixing

114   ratios than at high NO, the theoretical estimates are much greater than observed, suggesting that

115   additional losses reduce CH_3OOH in reality. In the DC3 environment, NO mixing ratios were

116   rarely (if at all) this low. However, the reverse situation could exist where increases in NO

117   mixing ratios from lightning production enable peroxy radicals to react with NO instead of with

118   each other, thereby preventing the formation of peroxides.

119

120   Although H_2O_2 is highly soluble, its partitioning between gas and aqueous phases, as well as that

121   for CH_3OOH, should be in Henry's law equilibrium based on theoretical calculations and

122   analysis of field measurements [Barth et al., 1989; MacDonald et al., 1995]. Because the Henry's

123   law equilibrium coefficients for H_2O_2 are over two orders of magnitude higher than those of

124   CH_3OOH, we expect that more H_2O_2 than CH_3OOH will be removed by cloud and precipitation

125   than CH_3OOH. However, we will show that CH_3OOH is sometimes removed more than

126   expected, even as much as H_2O_2.

127

128   In this paper we examine the behavior of CH_3OOH and H_2O_2 observed during DC3.   The

129   scavenging efficiencies of H_2O_2 and CH_3OOH are derived from measurements of these

130   peroxides and tracers of transport that were collected during the DC3 field experiment. The DC3

131   campaign and the instrument techniques used in the analysis are described in the next section.

132   We then present the analysis method for determining each storm's entrainment rate and the

133   peroxide scavenging efficiencies. We also use cloud-resolved 3-dimensional and box model

134   simulations to investigate physical and chemical processes affecting the peroxide scavenging.

135   Results for six DC3 storm cases are presented. In addition to discussing the uncertainties of the

6

136 calculations, we show how the peroxide scavenging efficiencies vary with some key storm

137 parameters, including the storm physics and chemistry.

138

139 **2. Methods**

140 **2.1 Observations**

141 The DC3 field experiment took place in May and June 2012, sampling thunderstorms in

142 northeast Colorado, west Texas to central Oklahoma, and northern Alabama. Ground-based

143 facilities documented the storm kinematics, physical structure, and lightning location. Three

144 aircraft, the NASA DC-8, the NSF/NCAR Gulfstream V, and the DLR Falcon 20, sampled the

145 inflow and outflow regions of the storms to quantify the composition of these regions. Barth et

146 al. [2015] present further details on the DC3 field experiment. In this paper, we utilize the data

147 from the NASA DC-8 aircraft to examine the scavenging of hydrogen peroxide and methyl

148 hydrogen peroxide in thunderstorms. While NSF/NCAR GV peroxide data are also available,

149 reconciling differences between the DC-8 and GV peroxide measurements are beyond the scope

150 of this paper. The DC-8 data are analyzed because the DC-8 flew in both inflow and outflow

151 regions for each case analyzed (whereas the GV flew most often in outflow regions).

152

153 The DC8 aircraft was extensively instrumented with trace gas and aerosol instruments [Barth et

154 al., 2015]. A list of the data and instruments used in this study is given in Table 1. Horizontal

155 winds, temperature, and pressure measurements on the DC-8 were obtained via the

156 meteorological measurement system (MMS). Ice water content (IWC) was measured onboard the

157 DC-8 aircraft by the SPEC 2-dimensional Stereo (2DS) probe [Lawson et al., 2006].

158

159   On the DC-8 aircraft H_2O_2 and CH_3OOH were measured using time-of-flight (ToF-CIMS) mass

160   filter and tandem quadrupole mass filter (T-CIMS) chemical ionization mass spectrometers

161   (CIMS), respectively. The rapid-scan collection of the ToF-CIMS instrument provides high

162   temporal resolution (1 Hz or faster) and simultaneous data products for all masses [Nguyen et al.,

163   2015]. The T-CIMS provides parent-daughter mass analysis, enabling measurement of

164   compounds precluded from quantification by a single mass analyzer CIMS due to mass

165   interferences (e.g. CH_3OOH) or the presence of isobaric compounds (e.g. isoprene oxidation

166   products) [Paulot et al., 2009; St. Clair et al., 2010]. Calibrations for H_2O_2 and CH_3OOH are

167   performed once per hour during flight using calibration standards for H_2O_2 (evolved from urea-

168   hydrogen peroxide) and CH_3OOH (from a diffusion vial). Note that the uncertainties for H_2O_2

169   (>50%) and CH_3OOH (~80% at low altitude and ~40% at high altitude) are high and contribute

170   the largest uncertainty to the analysis performed in this study.

171

172   The non-methane hydrocarbons n-butane, i-butane, n-pentane, and i-pentane are used to estimate

173   the entrainment rate for each storm. On the DC-8, these hydrocarbons were measured using the

174   whole air sampler (WAS), which pumps a sample of air into a previously evacuated canister with

175   an approximately 1 minute fill time (up to 2 minutes at high altitude) that is analyzed in the

176   laboratory by gas chromatography [Colman et al., 2010; Simpson et al. 2010]. Sampling

177   frequency is variable, but is typically every 2 to 5 minutes.

178

179   Aircraft measurements of OH, HO_2, sulfur dioxide (SO_2), NO, NO_2, and methyl peroxy nitrate

180   (MPN) are used in assessing whether CH_3OOH scavenging efficiencies are correlated with these

181   trace gases or to examine the gas-phase CH_3OOH production. The HO_x radicals, OH and HO_2,

8

182 were measured by the Pennsylvania State University Airborne Tropospheric Hydrogen Oxides

183 Sensor (ATHOS), which is a laser induced fluorescence technique [Faloona et al., 2004]. SO_2 is

184 measured with the Georgia Institute of Technology Chemical Ionization Mass Spectrometer

185 (CIMS) [Kim et al., 2007]. NO and NO_2 were measured with ozone-induced chemiluminescence

186 and ultra-violet photolysis of NO_2 to NO followed by ozone-induced chemiluminescence,

187 respectively [Pollack et al., 2011]. The NO_2 data before June 11, 2012 are from the University of

188 California – Berkeley thermal dissociation-laser induced fluorescence (TD-LIF) instrument

189 [Thornton et al., 2000; Nault et al., 2015]. Methyl peroxy nitrate mixing ratios were also

190 measured with the TD-LIF instrument as described by Nault et al. [2015].

191

192 Next Generation Weather Radar (NEXRAD) program Weather Surveillance Radar – 1988

193 Doppler (WSR-88D) data [Crum and Alberty, 1993] are used to understand the storm structure

194 and to estimate the distance of the DC-8 aircraft sampling the outflow from the nearest storm

195 core. Data from multiple radars, which are S-band (10 cm wavelength) radars, are processed to

196 produce 3-dimensional composites following the procedure described in Homeyer [2014] and

197 updated in Homeyer and Kumjian [2015]. Radiosonde data from soundings launched in the pre-

198 storm environment are used to determine the thermodynamic environment of the storm.

199 Radiosondes in Colorado are from the NCAR Mobile Integrated Sounding System and those in

200 Oklahoma from the National Severe Storms Laboratory (NSSL). The National Weather Service

201 North Platte sounding was used for the May 18 storm observed in southwest Nebraska. The

202 convective available potential energy (CAPE), 0-6 km vertical wind shear, depth from cloud

203 base to the freezing level, and depth from the freezing level to the -40°C isotherm were

204 calculated from the soundings. The CAPE is determined using mixed layer mean temperature,

205 where the mixed layer is defined between the surface and 100 hPa above the surface.

206

207 Six case studies were chosen from the DC3 dataset (Table 2) based on the type of convection and

208 the availability of DC-8 inflow and outflow data. Four of these cases were in the northeast

209 Colorado and southwest Nebraska region, and two were in Oklahoma. The cases are primarily

210 severe convection, with CAPE ranging from 900 to 3100 J kg^{-1}, and 0-6 km vertical wind shear

211 range of 12-24 m s^{-1}. The depth of the cloud where T > 0°C (where only liquid water cloud

212 physics occurs) varies substantially among storms. The Colorado convective storms have much

213 shallower depths between cloud base and the freezing level than Oklahoma convection, but this

214 depth increases from mid-May to late June. The depth from the freezing level to T = -40°C,

215 which is the temperature where cloud drops homogeneously freeze, is fairly consistent among

216 storms with depths from 4900 to 5200 m for Colorado storms and ~5800 m for Oklahoma

217 storms.

218

219 **2.2 Analysis Method**

220 Calculations of scavenging efficiencies from aircraft observations have been done previously by

221 using a multi-component mixture model. Cohan et al. [1999] considered two components, one

222 being the inflow region and the second being the upper troposphere where the convective

223 outflow resides. Borbon et al. [2012] used three components (BL, free troposphere, and UT) and

224 Yang et al. [2015] used four components (BL, buffer layer, clean layer, and UT, where the buffer

225 layer extends from the BL to 7 km altitude and the clean air layer extends from 7 km to 9.5 km

226 where the UT layer begins), adding entrainment of free troposphere air. Luo et al. [2010]

10

227   estimated entrainment in every 1 km layer of the deep convection. Here, and in Fried et al.

228   [2015], we combine the methods of these previous studies to determine the scavenging

229   efficiencies of trace gases.

230

231   Measurements from the inflow and outflow regions of the storm, as well as the free troposphere,

232   were used to compute the scavenging efficiencies. The DC-8 aircraft gathered these observations

233   by first sampling the inflow BL composition at several altitudes including a flight leg above the

234   BL top, then spiraling up to the anvil outflow region where several across-anvil passes were

235   made (Figure 1). Often the anvil passes were several kilometers downwind of the storm core tops

236   in order to keep the aircraft in a safe location from damaging hail and turbulence. Thus, some

237   degree of anvil dilution and chemistry is imparted on the trace gas mixing ratios before the DC-8

238   aircraft collects the measurements. To minimize the impact of dilution and chemistry, we use

239   outflow data that are closest to the storm core tops. Fried et al. [2015] employed a similar data

240   analysis, but instead used 1-minute averaged data in the outflow flight segments to extrapolate

241   back to the storm core top.

242

243   The aircraft sampling of the inflow and outflow regions was found by identifying flight segments

244   where horizontal winds showed air flowing into the storm within the boundary layer and air

245   flowing away from the storm cores in the anvil. Besides the physical location of the plane, the

246   chemical signatures of CO, hydrocarbons, and IWC were used to identify these flight legs.

247   Figure 2 illustrates the outflow legs used in the analysis for the six convection cases. For each

248   case, 20 minutes of the DC-8 flight track is plotted over the column maximum radar reflectivity.

249   The DC-8 flight track is colored by the magnitude of the CH_3OOH 30-s averaged mixing ratio.

250   The wind vectors (data from the DC-8) are plotted for the segment of the flight track used for the

251   outflow analysis. The inflow and outflow times for each of the cases are listed in Table 3. The

252   distance between the aircraft and storm cores varied among the different storm cases, with some

253   cases (e.g. May 29 in Figure 2b) just a few km from the cores developing in the anvil region and

254   others (e.g. June 22 in Figure 2f) nearly 100 km from the storm core.

255

256   Once the inflow and outflow time periods were identified, the average mixing ratios for several

257   trace gases were calculated. In some cases, mixing ratios were not available because of in-flight

258   calibration of the instrument. For example, on 18 May 2012, the inflow CH_3OOH mixing ratio

259   was estimated based on nearby flight legs. Specifically for this case, an estimate of the CH_3OOH

260   at 1.68 km was obtained by dividing the H_2O_2 mixing ratio at 1.68 km by the H_2O_2 to CH_3OOH

261   ratio at 2.57 km (which is ~1.2).

262

263   To obtain information on air entraining into the storm, a vertical profile of cloud-free data from

264   the storm region was obtained. Stratospheric air was omitted by removing times where the O_3 to

265   CO ratio was greater than 1.25. This method may not remove all of the data points with

266   stratosphere influence because of mixing of air caused by the thunderstorms as described in

267   recent studies [Schroeder et al., 2014; Huntrieser et al., 2015a,b]. Also removed from these

268   profiles were measurements of other unique features such as biomass burning plumes. These

269   were removed by restricting the time frame for the profiles, which was determined from the high

270   CO mixing ratios. Most of the cloud-free profiles are based on the DC-8 spiral from the

271   boundary layer to the upper troposphere. The data were binned into 1 km altitude ranges.

272   Missing data (because of in-flight calibrations and zeros) were filled in by interpolating to the

273   altitude of the missing data from the averages found above and below that altitude, and

274   extrapolating to the lowest or highest altitude if needed. Figure 3 shows cloud-free vertical

275   profiles of H_2O_2, CH_3OOH, n-butane, i-butane, n-pentane, and i-pentane for the six cases.

276

277   Cloud-free profiles of n-butane, i-butane, n-pentane, and i-pentane were used to estimate the

278   entrainment rate. These VOCs have chemical lifetimes (3-5 days) much longer than the time for

279   convective transport from the BL to the UT (typically 10-15 minutes [Skamarock et al., 2000])

280   and transport downwind to the aircraft (typically 30-45 minutes). Long chemical lifetimes and

281   very low solubility allow these VOCs to be markers of transport only. Fried et al. [2015] further

282   discuss the merits of using these tracers. The entrainment model follows an air parcel from just

283   below cloud base (CB), where that air has a VOC mixing ratio representing the BL, to the

284   location of the aircraft anvil measurements, where the VOC mixing ratio is a combination of the

285   VOC from the BL and the cloud-free (CF) VOC mixing ratios that are entrained into the storm.

286   The entrainment rate E (% km^{-1}) is found by calculating the VOC mixing ratio at 1-km altitude

287   bins from just below cloud base to the height of the aircraft measurements. For example, the

288   VOC mixing ratio at one km above cloud base ($VOC(z_{CB+1})$) is a combination of the VOC

289   mixing ratio at cloud base ($VOC(z_{CB})$) and the VOC in the cloud-free air at one km above cloud

290   base $VOC_{CF}(z_{CB+1})$ based on the fraction entrained. This equation can be generalized by the

291   following equation,

292
293 $$VOC(z) = E\,VOC_{cf}(z) + (1-E)\,VOC(z-1) \hspace{2cm} (1)$$

294

295   where $VOC(z)$ is the n-butane, i-butane, n-pentane, or i-pentane mixing ratio in the updraft at

296   each 1-km altitude z (km), $VOC(z-1)$ is the VOC mixing ratio at 1 km below the altitude z, and

13

297   $VOC_{cf}(z)$ is the average VOC mixing ratio in the cloud-free region at each 1-km altitude z. To

298   determine E, equation 1 was iterated until the calculated VOC mixing ratio at the height of the

299   aircraft outflow measurements and the measured VOC mixing ratio in the outflow region

300   matched within 1-10%. This procedure was conducted for all four VOCs and the average of

301   these derived entrainment rates were used to calculate the scavenging efficiency. The highest to

302   lowest entrainment rates give the range of entrainment rates for each storm and are used in

303   expressing the entrainment rate uncertainty. It is assumed that the entrainment rate is the same at

304   every 1 km altitude, however we estimate the impact of this assumption by utilizing variable

305   entrainment rates determined in the WRF simulation for the 29 May DC3 case in Section 3.

306

307   The first step in obtaining the scavenging efficiency of a soluble trace gas having mixing ratio

308   C_{sol} is to determine C_{sol} at the height of the aircraft outflow measurements ($C_{sol}(z=top)$) if it were

309   only transported (i.e. there is no dissolution into cloud particles and chemistry does not affect the

310   mixing ratio of C_{sol}). $C_{sol}(z=top)$ is found by using equation 1 with H_2O_2 or CH_3OOH in place of

311   the VOC and using the average entrainment rate. The scavenging efficiency SE (%) is found by

312   calculating the difference between the soluble trace gas mixing ratio measured from the aircraft

313   $C_{sol}(outflow)$ and the estimated transported mixing ratio at the height of the aircraft $C_{sol}(z=top)$

314   using,

315

316
$$SE = 100 \frac{C_{sol}(z=top) - C_{sol}(outflow)}{C_{sol}(z=top)} \qquad (2)$$

317

14

318   The uncertainty for C_{sol}*(outflow)* is the average uncertainty of the measurements in the outflow

319   flight leg. The uncertainty for the scavenging efficiency and C_{sol}*(z=top)* are found by the

320   quadrature method (Taylor, 1982).

321

322   While equation 2 is defining the scavenging efficiency, which is viewed as the physical removal

323   of a trace gas via dissolution and rain out, the equation actually encompasses all physical and

324   chemical processes occurring between the inflow and outflow regions sampled by the aircraft.

325   Thus, there can be physical removal, chemical destruction or even a reduction in chemical

326   production. An example of the last process, mentioned in the introduction and discussed in

327   Section 4, is the reduction in peroxide formation because the peroxy radicals react with NO to

328   form NO_2 and CH_2O instead of reacting with each other to form the peroxides.

329

330   **2.3 Description of Cloud-Resolving Scale Model Simulations**

331   The 29 May 2012 northern Oklahoma storm has been simulated with the Weather Forecasting

332   and Research model coupled with Chemistry (WRF-Chem [Grell et al., 2005]). Bela et al. [2015]

333   give a full description of the model configuration and simulation results. Table 4 provides

334   information on the WRF-Chem configuration. The model domain is centered on northern

335   Oklahoma using 1-km horizontal grid spacing and 88 vertical levels to 50 hPa (~20 km). The

336   cloud resolving grid spacing allows for explicit representation of transport and wet deposition in

337   the deep convection. The wet deposition scheme [Neu and Prather, 2012] estimates wet removal

338   of soluble trace gases from the gas phase. This scheme estimates trace gas removal by

339   multiplying the effective Henry's Law equilibrium aqueous concentration by the net

340   precipitation formation (conversion of cloud water to precipitation, minus evaporation of

341   precipitation). In mixed-phase conditions (258 K < T < 273 K), the Neu and Prather [2012]

342   scheme estimates a fraction of the dissolved gas to be retained in the frozen hydrometeors. The

343   retention fraction of H_2O_2 and CH_3OOH is set to 0.64 and 0.01, respectively, in accordance with

344   laboratory values compiled by Leriche et al. [2013]. Other soluble trace gases (CH_2O, HNO_3,

345   and SO_2) also use retention factors recommended by Leriche et al. [2013], while all other trace

346   gases are completely degassed from the condensed phase. Sensitivity simulations were

347   conducted to explore the effect of the retention factor on trace gas scavenging.

348

349   In addition to the simulations that included wet deposition, a simulation without wet deposition

350   was performed. The scavenging efficiencies (SE) are then calculated from these results using the

351   following equation.

352

353
$$SE = 100 \frac{(C_{noscav} - C_{scav})}{C_{noscav}} \qquad (3)$$

354   where C_{noscav} and C_{scav} are average model mixing ratios of soluble trace gas C near the storm core

355   as defined by the eastern (i.e., downwind) 40 dBZ maximum reflectivity contour. This location

356   was chosen based on the analysis method of the observations outlined above. For the 29 May

357   DC3 case, the DC-8 measurements were obtained near storm cores with reflectivity > 40 dBZ

358   (Figure 2b). The mixing ratios of the trace gases were averaged in the convective outflow

359   altitudes (9.43-11.59 km).

360

361   In another simulation, 20 tracers representing air in each 1-km altitude layer of the atmosphere

362   from the surface to the top of the model (~20 km). These layer tracers were set to a value of 1.0

363   in their respective layer for a 10-minute time period (0010-0020 UTC 30 May 2012) and

16

364   analyzed 2 hours after the initialization of the tracer at 0200 UTC 30 May 2012 to allow time for

365   boundary layer air to reach the outflow location. The results were analyzed to determine the

366   percent contribution of each layer to the modeled storm core top as defined above. These percent

367   contributions from each layer (Table 5) were used as the entrainment rate for calculations of

368   scavenging efficiency from the aircraft observations to compare results from an average

369   entrainment rate with those from an altitude-varying entrainment rate in Section 3.

370

371   **2.4 Box Model Calculations**

372   The gas-aqueous chemistry box model described by Barth et al. [2003] is used to analyze the

373   chemistry within the updraft regions of a severe thunderstorm. The box model has been modified

374   to include the non-methane hydrocarbon gas-phase chemistry described by Kim et al. [2012].

375   The aqueous-phase chemistry represents only S(IV), O_3, H_2O_2, and CH_2O chemistry [Barth et al.,

376   2007a]. Other soluble VOC trace gases, e.g. organic aldehydes, peroxides, and nitrates, also

377   partition into the aqueous phase following Henry's Law equilibrium, but do not undergo

378   aqueous-phase chemistry. The coefficients for Henry's Law are from Sander [2015] and Sander

379   et al. [2011]. Photolysis rates are appropriate for 36°N beginning at 00 UTC (1900 local time),

380   matching the time of the storm observations. The photolysis rates vary with altitude and are

381   modified by cloud scattering assuming a cloud optical depth of 500, cloud base of 2 km and

382   cloud top of 15 km. The photolysis rates are less than their clear sky values throughout the

383   simulation as depicted by the cloudy to clear sky H_2O_2 photolysis rate ratio in Figure 4b.

384

385   The box model has also been modified to have varying liquid water content, temperature,

386   pressure, and altitude, which are prescribed using results from the WRF-Chem simulation at 00

387 UTC 30 May 2012. Values are averages at each model level within the 36°N-37°N and 99°W-

388 97°W latitude and longitude region and where vertical velocity in the column exceeds 5 m s^{-1}.

389 The resulting cloud hydrometeor vertical profiles are shown in Figure 4a. For the box model

390 simulations we prescribe only the cloud liquid water content and exclude the water content from

391 precipitation. From Figure 4, it is evident that much of the condensed water is in the

392 precipitation, primarily as hail, for this updraft region. Because the box model calculations are a

393 function of time, the prescribed time coordinate is converted to an altitude coordinate so that the

394 chemistry of a hypothetical rising air parcel can be determined. The air parcel begins at the 1.16

395 km altitude (near cloud base), solves for only gas-phase chemistry for 10 minutes to allow the

396 radicals to reach approximate photochemical equilibrium, then is lifted to higher altitudes

397 assuming a 3 m s^{-1} updraft. At ~14 km where the WRF-Chem updraft velocities are ~0 m s^{-1}, the

398 artificial lifting of the box is stopped. The 14 km altitude is above the cloud water region of the

399 storm (Figure 4); the top of the cloud water region is 10.9 km. Thus, the air parcel undergoes just

400 gas-phase chemistry between 10.9 and 14 km.

401

402 To determine if H_2O_2 and CH_3OOH would be depleted if only gas-phase chemistry were

403 occurring, a box model simulation with no liquid water was performed. Figure 4 shows that

404 H_2O_2 and CH_3OOH have similar mixing ratios at cloud base (2.2 ppbv for H_2O_2 and 1.46 ppbv

405 for CH_3OOH). Thus, for the conditions of the box model simulation, both peroxides are not

406 produced by the gas-phase chemistry. A second simulation with the prescribed LWC show that

407 in the cloud water region (2-11 km altitude) gas-phase H_2O_2 is rapidly depleted, with mixing

408 ratios reduced to <0.2 ppbv in the mixed cloud region (4-11 km altitude). Note that solubility

409 constants increase as temperature decreases, allowing more of the soluble trace gas to partition

18

410   into the aqueous phase. Gas-phase CH_3OOH mixing ratios also decrease, but by <10% of the

411   gas-phase only simulation. At the top of the cloud water region, the peroxides in the aqueous

412   phase return to the gas phase because of the lack of liquid water. In an actual cloud the cloud

413   water is more likely being collected by precipitating cloud particles and freezing. Thus, what is

414   shown in Figure 4 is akin to the trace gases being degassed from all cloud particles. In summary,

415   simple partition theory based on Henry's law equilibria and gas- and aqueous-phase chemistry

416   suggests substantial depletion of gas-phase H_2O_2 and small depletion of CH_3OOH. Gas-phase

417   chemistry alone does not deplete either H_2O_2 or CH_3OOH appreciably during transit from cloud

418   base to cloud top.

419

420   **3. Results**

421   Average mixing ratios for H_2O_2 and CH_3OOH measured during the DC8 flight inflow and

422   outflow time periods are listed in Table 6. The mixing ratios in the inflow region are always

423   higher than those in the outflow for both peroxide species, indicating that net production of

424   peroxides within the storm is not occurring. The inflow mixing ratios vary from case to case,

425   suggesting a dependence on vicinity to anthropogenic sources and time of year. The 18 May and

426   22 June storms, with lower H_2O_2 mixing ratios, both occurred near the Wyoming-Colorado-

427   Nebraska border further from the Front Range urban region than the 2 June and 6 June Colorado

428   cases. The average NO_x mixing ratios for the 29 May, 2 June, 6, June, and 16 June inflow air

429   were 400-650 pptv, whereas that for the 22 June storm was ~260 pptv (the inflow NO_x mixing

430   ratio for the 18 May storm was not measured due to instrument issues). The outflow mixing

431   ratios also have some variability among the different storm cases. The uncertainties for the

432   average values can be quite large, ranging from 50-60% and 77-84% for H_2O_2 and CH_3OOH,

433   respectively, in the boundary layer inflow air and 80-175% and 49-70% for H_2O_2 and CH_3OOH,

434   respectively, in the outflow air.

435

436   The mixing ratios for the butanes and pentanes in the inflow air (Table 7) vary from storm to

437   storm, but the variation is not correlated to the variation found for the peroxides. Higher mixing

438   ratios in both the inflow and outflow air occur over Oklahoma than in Colorado, except for the

439   18 May case. The outflow mixing ratios are often much smaller than the inflow mixing ratios,

440   except for the 22 June outflow where mixing ratios are only slightly less than those in the inflow

441   suggesting less entrainment in the 22 June storm. Note that the 6 June case uses butane and

442   pentane mixing ratios extrapolated to the storm top as determined by Fried et al. [2015] because

443   the DC-8 mixing ratios from the outflow period listed in Table 5 have anomalously high butane

444   and pentane mixing ratios that are greater than the inflow mixing ratios. Instead of using DC-8

445   data from outflow near the edge of the storm (and quite far from the storm cores), we chose to

446   use the mixing ratios determined from a combination of DC-8 and GV data [Fried et al., 2015].

447

448   The i-butane/n-butane and i-pentane/n-pentane ratios also provide evidence that the air measured

449   by the DC-8 in the inflow region of the storms is connected to that sampled in the outflow region

450   in the storm anvils. Gilman et al. [2013] and Swarthout et al. [2013] explain that these ratios are

451   limited to a small range of values for a given source (e.g. cities, biomass burning emissions, oil

452   and gas emissions). However, the ratios from source to source varies, where the i-butane/n-

453   butane ratio is found to be 0.48 for U.S. cities, 0.26-0.27 for biomass burning emissions, 0.36-

454   0.69 for oil and gas emissions, and i-pentane/n-pentane ratio is 2.0 for U.S. cities, 0.31-0.37 for

455   biomass burning emissions, and 1-1.4 for oil and gas emissions in the Texas, Oklahoma, Kansas

20

456 region [Blake et al., 2015; Fried et al., 2015]. These ratios should be maintained for several hours

457 because their rate constants with OH are within 10-15% for n-butane and i-butane oxidation and

458 within 10% for n-pentane and i-pentane oxidation. The i-butane/n-butane and i-pentane/n-

459 pentane ratios for the inflow regions of all the storms analyzed for this study lie within the range

460 for oil and gas emissions as found by Blake et al. [2015] and Gilman et al. [2013] for the Texas,

461 Oklahoma, and Kansas region. This is not a surprising result because both Oklahoma and

462 northeast Colorado have active oil and gas operations. The i-butane/n-butane and i-pentane/n-

463 pentane ratios are fairly consistent between inflow air and outflow air for each storm, although

464 some differences occur possibly because the storm is entraining air with different i-butane/n-

465 butane and i-pentane/n-pentane ratios than the inflow region. Nevertheless, these ratios indicate

466 that the two air masses sampled are well connected between inflow and outflow of each storm.

467

468 Entrainment rates, as calculated via the method described in Section 2.2, range from 4.1% km^{-1}

469 to 17.2% km^{-1} for the different storms analyzed (Table 8). The entrainment rate for 6 June was

470 obtained from Fried et al. [2015] because the VOCs measured by the DC-8 were anomalously

471 high in the outflow region. The entrainment rates for three of the cases are similar to those found

472 by Luo et al [2010] who used moist static energy profiles to determine entrainment rates of

473 <10% km^{-1} for deep convective tropical, oceanic cumulus clouds. Moreover, the entrainment rate

474 for the May 29 storm is identical to that found by Fried et al. [2015]. The entrainment rate for the

475 June 22 storm is within the mutual precision limits of Fried et al. [2015] who estimated 3.1 ±

476 1.1% km^{-1} compared to 4.8 ± 0.9% km^{-1} in this study. The small difference for the June 22 storm

477 is expected since Fried et al. [2015] extrapolate their outflow data to estimate mixing ratios at

478 storm core top, which are generally higher than the average values closest to the storm core

479   employed here. If the entrainment rates reported in Table 8 are integrated for a 9 km depth, the

480   total storm entrainment rate range is 40-68%, which is similar to entrainment rates of

481   midlatitude, continental convection [Barth et al., 2007a; Thompson et al., 1994] and subtropical

482   convection [Scala et al., 1990]. The entrainment rates determined here tend to be smaller for

483   storms with higher 0-6 km vertical wind shear (Table 2), although the 16 June Oklahoma case

484   has a high vertical wind shear of ~16 m s^{-1} and a high entrainment rate. Both low-level vertical

485   wind shear and entrainment rate contribute to the storm intensity and longevity as they play a

486   role in the strength of the cold pool and tilt of the updraft [Weisman et al., 1988; Lee et al.,

487   2008].

488

489   The calculated scavenging efficiencies for H_2O_2 and CH_3OOH for each storm analyzed range

490   from 79% to 97% and 12% to 84%, respectively (Table 8). While there is some variability of

491   scavenging efficiency among storms for H_2O_2, there is much more variability for CH_3OOH. The

492   H_2O_2 scavenging efficiencies estimated from DC3 storms are somewhat greater than those

493   previously found. Numerical modeling of a low-precipitation supercell observed in northeast

494   Colorado yielded a 57% H_2O_2 scavenging efficiency [Barth et al., 2007a]. Wang [2005]

495   estimated H_2O_2 scavenging efficiencies of 88-90% for tropical deep convection. Global

496   chemistry transport model simulations estimated that a soluble species with a Henry's Law

497   coefficient similar to H_2O_2 has a 90% scavenging efficiency in deep convection [Crutzen and

498   Lawrence, 2000]. Estimated H_2O_2 scavenging efficiency, based on boundary layer, convective

499   outflow, and UT background observations, for an oceanic, tropical convective storm is 55-70%

500   [Cohan et al., 1999]. CH_3OOH scavenging efficiencies for DC3 storms are also greater than past

22

501 results. Barth et al. [2007a] determined a 7% scavenging efficiency, while Cohan et al. [1999]

502 found no significant scavenging of CH_3OOH.

503

504 The most surprising result is the substantial scavenging of CH_3OOH for two of the storms (29

505 May and 6 June) of greater than 75%, which is much greater than what is expected based on

506 Henry's Law equilibrium between the gas and aqueous phases as shown in Section 2.4.

507 However, the cloud physics in deep convective clouds is much more complicated than the simple

508 model of a liquid-only cumulus cloud. The ice phase in deep convection interacts with the cloud

509 and rain drops through freezing and melting processes, and the fate of the dissolved trace gas is

510 uncertain when freezing occurs [Barth et al., 2001; 2007a], but is related to the value of the trace

511 gas Henry's Law and the time it takes a drop to freeze [Stuart and Jacobson, 2006]. Other storm

512 characteristics (e.g. entrainment) can also affect the scavenging rate of the trace gas. Some of

513 these effects will be discussed in the next section.

514

515 It is important to realize that the uncertainty in the estimated scavenging efficiencies is large and

516 is mostly a product of the uncertainties of the peroxide measurements. The peroxide uncertainties

517 are 50% or greater for H_2O_2 and ~80% for low altitude and 40% or greater for high altitude

518 CH_3OOH (Section 2, Table 6). The high uncertainties propagate to the scavenging efficiencies,

519 manifesting into 5-23% uncertainty in the H_2O_2 scavenging efficiency and 15-67% uncertainty in

520 the CH_3OOH scavenging efficiency. For CH_3OOH, there tends to be more uncertainty associated

521 with the lower scavenging efficiencies.

522

523   In addition to the measurement uncertainties, there are uncertainties associated with the analysis

524   method. While much care was invested in quantifying relevant values in inflow and outflow air,

525   there exists the possibility that the times chosen include air that was not processed by the deep

526   convection. A major assumption of the analysis is that the entrainment rate is constant for each

527   kilometer layer from cloud base to the top of the storm cell. To test this assumption, the WRF-

528   Chem model run using tracers described in Section 2.3 was analyzed to provide an altitude-

529   dependent entrainment rate (Table 5) for the 29 May severe convection case in Oklahoma. For

530   this case, the entrainment rate based on the hydrocarbon analysis was estimated to be 7.6%,

531   while the WRF-Chem model estimated an average entrainment rate for the 1-11 km altitude

532   range of 7.3%. Thus, the average entrainment rates based on these two methods are similar.

533   However, the model results give a variation of entrainment with height, with higher entrainment

534   in the first 2 kilometers near cloud base and near 7 km and the lowest entrainment from 3-5 km

535   altitude and above 9 km altitude (Table 5). By using the altitude-dependent entrainment rates for

536   estimating the scavenging efficiency, we obtain values of 89% and 80% scavenging for H_2O_2

537   and CH_3OOH, respectively. These values are similar to the 88% and 77% estimated by the

538   constant entrainment rate method and are well within the uncertainty.

539

540   A comparison of WRF-Chem simulations with and without wet deposition was done to estimate

541   scavenging efficiencies for the 29 May northern Oklahoma storm. Average H_2O_2 and CH_3OOH

542   mixing ratios at the eastern edge of the modeled storm core tops, which was defined in

543   longitude-latitude space by the column maximum radar reflectivity of 40 dBZ, were found for

544   each of the simulations. Bela et al. [2015] explore the sensitivity of the scavenging efficiency to

545   the retention of the dissolved trace gas in freezing drops. They find that the H_2O_2 scavenging

24

546   efficiency to be 100% with retention fractions into ice of 0.25, 0.5, 0.64, and 1.0 and 78±11% for

547   when there is no retention of dissolved trace gas in freezing drops. For CH_3OOH, Bela et al.

548   [2015] find the scavenging efficiency to be 26±6%, 35±7%, 39±5%, 51±4%, and 61±3% for

549   retention fractions of 0, 0.02, 0.25, 0.5, and 1.0, respectively. The model results with 100%

550   retention for CH_3OOH in ice give a CH_3OOH scavenging efficiency (61%) most similar to the

551   value calculated from observations (77%). In contrast, the simulation with 0% retention in ice

552   produced CH_2O mixing ratios in the convective outflow that best matched the observations

553   [Fried et al., 2015]. Further analysis is being done to investigate the potential role of aqueous-

554   phase chemistry on peroxide mixing ratios. These results suggest the retention of H_2O_2 and

555   CH_3OOH in freezing drops is an important contribution to scavenging of peroxides.

556

557   **4. Discussion**

558   Here, we seek to get an idea of what atmospheric processes contribute to the wide range of

559   CH_3OOH scavenging that can be used as guidance in future analysis. Both physical processes

560   and chemical transformations can affect the H_2O_2 and CH_3OOH mixing ratios in thunderstorms.

561   The thermodynamic environment in which the storms form determines the storm morphology.

562   However, key cloud physical processes affecting the soluble trace gases are the liquid water

563   content and the production of graupel and hail. As the air parcel is ingested and lofted to the top

564   of the storm and then carried into the anvil region, the soluble trace gases undergo chemical

565   transformations in both the gas and aqueous phases. All of these factors must be considered in

566   terms of understanding the estimated H_2O_2 and CH_3OOH scavenging efficiencies. Since derived

567   CH_3OOH scavenging efficiencies vary so much, the discussion focuses on CH_3OOH.

568

569   The thermodynamic environment is critical for determining the storm morphology and intensity.

570   Two important parameters of the thermodynamic environment are the convective available

571   potential energy (CAPE) and the low-level vertical wind shear [Weisman and Klemp, 1982]. For

572   DC3 storm cases, Barth et al. [2015] showed that the Alabama cases resided in the low shear and

573   low CAPE regime, the Oklahoma/Texas cases resided in the high shear and high CAPE regime,

574   while the Colorado cases resided between these two extremes. However, two Colorado cases had

575   both high vertical wind shear and high CAPE similar to the Oklahoma cases. Placing the

576   scavenging efficiencies in the context of the thermodynamic environment (Figure 5) shows that

577   there is no strong correlation of H_2O_2 scavenging efficiencies with CAPE and the 0-6 km vertical

578   wind shear. The same is true for CH_3OOH scavenging efficiencies, although the two highest

579   CH_3OOH scavenging efficiencies occur in severe storms with similar CAPE and vertical wind

580   shear parameters.

581

582   The morphology of the storm also depends on the depth of the warm cloud where only liquid

583   water resides and depth of the mixed phase region because the cloud physics processes differ in

584   these two regions. The Colorado storms have higher cloud bases than the Oklahoma storms

585   because the warm and dry boundary layers in the region require higher lifting condensation

586   levels. The Colorado storms have shallow warm cloud depths (Table 2), restricting the degree of

587   scavenging via collision and coalescence of cloud droplets. However, supercooled liquid water

588   can exist at temperatures down to 233 K (-40°C) and dissolution into the liquid from the gas

589   phase occurs much more readily at colder temperatures. Nevertheless, the calculated H_2O_2 and

590   CH_3OOH scavenging efficiencies showed no correlation with the warm cloud depth or depth of

591   cloud where cloud droplets exist. Further, the average ice water content (IWC) measured during

26

592 each outflow leg showed no correlation with the H_2O_2 and CH_3OOH scavenging efficiencies.

593 Fried et al. [2015] found the same lack of correlation between CH_2O scavenging efficiencies and

594 IWC and did not see substantial differences of CH_2O scavenging efficiencies between types of

595 storms except possibly the weak convection observed in Alabama that had a high CH_2O

596 scavenging efficiency.

597

598 The amount of entrainment estimated for each storm may affect the CH_3OOH scavenging

599 efficiency. For five out of the six storms, there is an increase in scavenging efficiency with a

600 decrease in entrainment (Figure 6). Entrainment brings into the storm free troposphere

601 background mixing ratios that are lower than those at the top of the boundary layer resulting in a

602 reduction in CH_3OOH mixing ratios in the updraft regions. When there is more entrainment,

603 more low mixing ratios are mixed into the updraft region than when entrainment rates are lower.

604 The possible importance of entrainment on convective outflow mixing ratios suggests that the

605 shape of the vertical profile of the peroxides may be important. For example, a rapid decrease in

606 mixing ratio from the top of the boundary layer into the free troposphere would decrease

607 CH_3OOH more than if the cloud-free mixing ratios remained elevated into the mid-troposphere
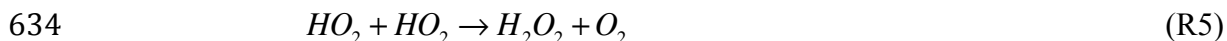
608 (e.g. June 16, Figure 3).

609

610 Another factor to consider is the chemistry that the peroxides experience as they are transported

611 from cloud base to the aircraft location in the anvil outflow region. Both H_2O_2 and CH_3OOH are

612 primarily destroyed by photolysis (R1, R2) and oxidation by OH (R3, R4).

613 $$H_2O_2 + hv \rightarrow 2OH \qquad\qquad\qquad (R1)$$

614 $$CH_3OOH + hv \rightarrow CH_2O + HO_2 + OH \qquad\qquad\qquad (R2)$$

615 $$H_2O_2 + OH \rightarrow HO_2 + H_2O \qquad \text{(R3)}$$

616 $$CH_3OOH + OH \rightarrow products \qquad \text{(R4)}$$
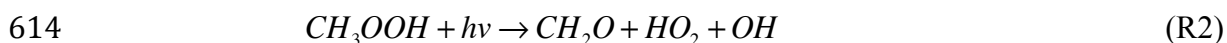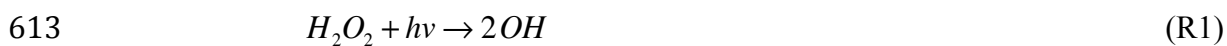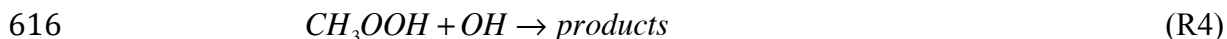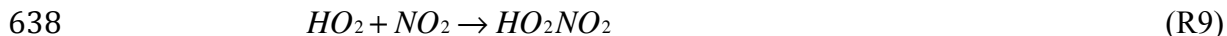
617 The rates of these reactions are altered by the presence of deep convection because the cloud

618 particles scatter incoming solar radiation. When the cloud is attenuating solar radiation causing

619 reduced photolysis rates and OH concentrations [Chang et al., 1987; Brasseur et al., 2002], the

620 photochemistry tends to proceed more slowly. However, near the top of cloud where it is much

621 brighter, the chemistry is accelerated. Because H_2O_2 and CH_3OOH are both produced and

622 destroyed by HO_x and photolysis rates, their gas-phase photochemistry is less certain when

623 clouds scatter radiation. Previous modeling studies showed a <5% effect on peroxide mixing

624 ratios caused by cloud modified photolysis rates for boundary layer clouds in a marine setting

625 [Barth et al., 2002]. However, Wang [2005] expected increases of H_2O_2 in the upper regions of

626 deep convection due to the decreased photolysis rates and lack of water in which H_2O_2 dissolves

627 and undergoes aqueous chemistry.

628

629 The production of H_2O_2 is primarily from the hydroperoxy radical self-reaction (R5). Similarly,

630 CH_3OOH is produced from methyl peroxy radical reaction with the hydroperoxy radical (R6).

631 However, NO reaction with the peroxy radicals and NO_2 reaction with peroxy radicals compete

632 with the peroxide production (R7-R10), causing less peroxide production at higher NO

633 concentrations.

634 $$HO_2 + HO_2 \rightarrow H_2O_2 + O_2 \qquad \text{(R5)}$$

635 $$CH_3OO + HO_2 \rightarrow CH_3OOH + O_2 \qquad \text{(R6)}$$

636 $$HO_2 + NO \rightarrow NO_2 + OH \qquad \text{(R7)}$$

637 $$CH_3OO + NO + O_2 \rightarrow NO_2 + CH_2O + HO_2 \qquad \text{(R8)}$$

28

638 $$HO_2 + NO_2 \rightarrow HO_2NO_2 \tag{R9}$$

639 $$CH_3OO + NO_2 \rightarrow CH_3OONO_2 \tag{R10}$$

640 In a thunderstorm, low NO conditions may exist in the inflow region of the storm, but as the air

641 parcel rises generation of NO from lightning would create a high NO situation. While the peroxy

642 radicals have other destruction reactions (e.g. $HO_2 + OH$, and reaction with other organic peroxy

643 radicals), their contribution to peroxy radical loss is much smaller than the reactions listed in R7-

644 R10. Comparing the loss of CH_3OO via reaction with HO_2 (R6) with those via reactions with NO

645 (R8) and NO_2 (R10) can illuminate whether the NO conditions are affecting the estimate of the

646 CH_3OOH scavenging efficiency. We can define the fraction of CH_3OO to produce CH_3OOH

647 (F_{Prod_CH3OOH}) as,

648 $$F_{Prod\_CH3OOH} = \frac{k_6[HO_2]}{k_6[HO_2] + k_8[NO] + k_{10}[NO_2]} \tag{4}$$

649 This fraction can be estimated using the DC-8 aircraft data for NO, NO_2, HO_2, and temperature.

650 The calculated F_{Prod_CH3OOH} values are found to be < 1% because of the high NO_x mixing ratios,

651 which ranged from 0.7 to 2.5 ppbv, and low HO_2 mixing ratios (0.3 – 3.9 pptv) measured in the

652 outflow flight legs. Comparing F_{Prod_CH3OOH} to the CH_3OOH scavenging efficiency (Figure 7a)

653 shows for five of the six storms analyzed there is a strong correlation ($r^2 = 0.90$) between the two

654 parameters, with more CH_3OOH scavenged when its fraction produced is less. The one storm

655 that did not correspond well with this trend is the June 16, 2012 Oklahoma storm when outflow

656 measurements were taken near sunset (measured photolysis rates were 2 orders of magnitude

657 smaller than the other DC3 cases analyzed).

658

659 Reaction 10 produces methyl peroxy nitrate (MPN), which was measured by the TD-LIF

660 instrument on the DC-8. A comparison of average MPN data in the outflow region with the

661   CH$_3$OOH scavenging efficiencies shows no correspondence between the two parameters when

662   all the storms are included in the comparison, but a strong correspondence between the two

663   parameters when the data from 18 May and 6 June Colorado storms are omitted (Figure 7b).

664   MPN measurements from these two storms were below detection limit. Nevertheless, the

665   correlation shown in Figure 7b suggests that lightning-generated NO$_x$ in the updraft region and

666   anvil is correlated with CH$_3$OOH mixing ratios in the anvil.

667

668   To learn whether NO production from lightning could be a potential reason for CH$_3$OOH

669   depletion in thunderstorm anvils, the gas-aqueous photochemical box model was used. The

670   model began with the same conditions as described in Section 2.4 but had a NO emission

671   included representing lightning-NO$_x$ production. The NO source was set to 10 pptv per time step

672   (10 s) from the altitude where T = 285 K to the altitude where T = 223 K. This profile is based

673   on the WRF-Chem results of NO mixing ratio in the updraft region. In Figure 8a, the NO vertical

674   profiles from the simulations without the "lightning-NO$_x$" source and with the "lightning-NO$_x$"

675   source are shown. The source of NO causes an increase of NO mixing ratios from ~0.1 ppbv to

676   ~1.2 ppbv. Even with the increase in NO mixing ratios, both gas-phase H$_2$O$_2$ and CH$_3$OOH

677   mixing ratios are unchanged from the simulations where the "lightning-NO$_x$" source was not

678   included (Figure 8b), although the change in CH$_3$OOH mixing ratios does show a <5 pptv

679   decrease. Despite the null result from the parcel model calculations, the correlations shown

680   above suggest that chemistry may play a role in affecting peroxide mixing ratios and cloud-

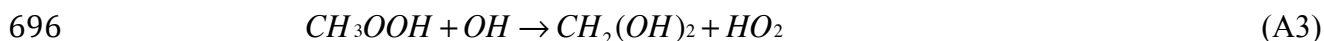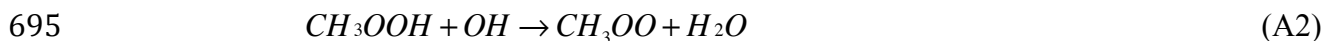681   resolving chemistry models could be used to examine this further.

682

683 The results from the observational analyses do not depend on the time since the air parcel exited

684 the storm core and was sampled by the DC-8 aircraft (Figure 7c), which was determined from

685 the distance the aircraft was from the storm core using Figure 2 and dividing by the horizontal

686 wind speed from the aircraft measurements. Indeed, the storms with the highest CH_3OOH

687 scavenging efficiencies, June 6 and May 29, have very different estimated times since the air

688 parcel exited the storm core of ~60 minutes and ~18 minutes, respectively.

689

690 Aqueous-phase chemistry can also affect CH_3OOH mixing ratios in a storm via in-cloud reaction

691 between CH_3OOH and HSO_3^- [Seinfeld and Pandis, 1998],

692 $$CH_3OOH + HSO_3^- + H^+ \rightarrow SO_4^{2-} + 2H^+ + CH_3OH \qquad \text{(A1)}$$
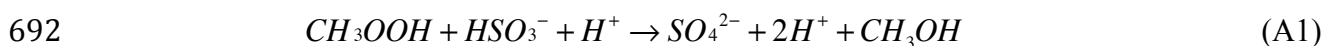
693 The hydroxyl radical OH can also oxidize CH_3OOH in the aqueous phase forming either CH_3OO

694 radicals or CH_2O.

695 $$CH_3OOH + OH \rightarrow CH_3OO + H_2O \qquad \text{(A2)}$$

696 $$CH_3OOH + OH \rightarrow CH_2(OH)_2 + HO_2 \qquad \text{(A3)}$$

697 Barth et al. [2007a] included reactions A2 and A3 in their cloud chemistry modeling of

698 thunderstorm chemistry and found essentially the same scavenging efficiency when aqueous

699 chemistry was included in the simulation as when aqueous chemistry was excluded. However,

700 Barth et al. [2007a] did not include reaction A1. To learn whether reaction A1 may be important,

701 the CH_3OOH scavenging efficiency is compared to the SO_2 inflow mixing ratios for each storm

702 case. Unfortunately SO_2 mixing ratios from the DC-8 are not available for the May 29 Oklahoma

703 storm because of instrument problems that day. The GV SO_2 measurements at low levels (2-3.5

704 km altitude) were obtained just before storm initiation but were primarily in western Oklahoma,

705 to the west of where the DC-8 inflow legs were. Thus, the low-level GV measurements were not

706 necessarily representative of the inflow conditions and are not used here. A comparison of the

707 CH_3OOH scavenging efficiencies with inflow SO_2 for the other five storm cases shows a strong

708 anti-correlation, with more scavenging at low SO_2 conditions (Figure 7d). Intuitively, this anti-

709 correlation seems to be the opposite of what is expected if aqueous-phase chemistry is reducing

710 CH_3OOH. While there is a strong anti-correlation between CH_3OOH scavenging efficiencies and

711 inflow SO_2, it is not obvious if SO_2 is affecting CH_3OOH mixing ratios in the storm outflow

712 region.

713

714 **5. Conclusion**

715 We have analyzed DC3 observations of hydrogen peroxide and methyl hydrogen peroxide to

716 determine their scavenging efficiencies in thunderstorms observed in the High Plains of northeast

717 Colorado and Southern Great Plains of Oklahoma. The analysis method, which is similar to that

718 described by Fried et al. [2015], first finds an entrainment rate for each storm by using mixing

719 ratios of n-butane, i-butane, n-pentane, and i-pentane, which are all sufficiently long-lived

720 chemically and insoluble to be good tracers of transport, in the inflow and outflow regions, and

721 clear-air vertical profiles. Once the entrainment rate is known, the peroxide scavenging

722 efficiencies are found from the measurements from the same inflow, outflow, and clear-sky

723 regions. The calculated H_2O_2 and CH_3OOH scavenging efficiencies are 79-97% and 12-84%,

724 respectively, for six DC3 storms analyzed. The scavenging efficiency uncertainties are 5-23%

725 and 15-67% for H_2O_2 and CH_3OOH, respectively, and are mostly from the uncertainties of the

726 peroxide measurements. The cloud resolving modeling by Bela et al. [2015] predicts scavenging

727 efficiencies similar to those observed for the 29 May 2012 DC3 storm when the retention

728 efficiency of H_2O_2 and CH_3OOH dissolved in freezing drops was 25% or greater for H_2O_2 and

32

729   100% for CH_3OOH. These modeling results suggest that the degree of riming of cloud drops by

730   snow and graupel could affect the amount of CH_3OOH scavenged by the storms.

731

732   We investigated several environmental, storm morphology, and chemical parameters that may

733   contribute to the wide range of calculated CH_3OOH scavenging efficiencies. While the

734   thermodynamic environment (e.g. CAPE and 0-6 km vertical wind shear) and physical processes

735   (e.g. ice water content) play a role in the degree of scavenging, they do not explain why

736   CH_3OOH scavenging has such a large range for the six storms examined. We found that more

737   CH_3OOH was scavenged at low entrainment rates and less CH_3OOH was scavenged at high

738   entrainment rates in storms. This correlation may be connected with the shape of the CH_3OOH

739   vertical profile in clear sky since the peroxide profiles usually did not decrease sharply with

740   altitude like the butane and pentane vertical profiles, from which the entrainment rate was

741   derived. Further, the variability of entrainment rate with height (as prescribed by the cloud

742   resolving model simulation) does not significantly change the calculated scavenging efficiencies.

743

744   The production of NO from lightning may influence CH_3OOH mixing ratios in the convective

745   outflow by increasing the $CH_3OO + NO$ and the $CH_3OO + NO_2$ reaction rates, which reduces the

746   production of CH_3OOH via $CH_3OO + HO_2$. Correlations between the CH_3OOH scavenging

747   efficiency and the fraction of CH_3OO producing CH_3OOH and between the scavenging

748   efficiency and methyl peroxy nitrate suggest such a connection. However, our gas-aqueous

749   photochemical box model shows that gas-phase CH_3OOH mixing ratios are unchanged when a

750   NO source is included in the simulation. CH_3OOH can also be destroyed in the aqueous phase

751   via reaction with bisulfite ion (the dominant form of SO_2 in cloud droplets), suggesting a positive

752   correlation between CH_3OOH scavenging efficiencies and the inflow SO_2 mixing ratios.

753   However, we found a strong anti-correlation between these two quantities indicating that the

754   aqueous-phase chemistry may not contribute to the wide range of scavenging efficiencies found.

755

756   The analysis done here, via correlations between measured variables and calculated scavenging

757   efficiency and process-scale modeling, suggests that dynamical, physical, and chemical

758   processes affect CH_3OOH in the outflow of thunderstorms. The amount of hail in the storm plays

759   an important role in two ways. First, the production of hail involves substantial riming of cloud

760   droplets by falling snow and graupel. A portion of a trace gas dissolved in the cloud droplets

761   would be retained in the precipitating hail and subsequently removed from the atmosphere. Hail

762   also plays a key role in triggering lightning. The NO produced from lightning reduces the

763   production of gas-phase CH_3OOH because of NO and NO_2 reactions with CH_3OO (a key

764   precursor of CH_3OOH) forming formaldehyde, NO_2, and methyl peroxy nitrate, as shown in

765   scatter plots between CH_3OOH scavenging efficiencies and two of these parameters. However,

766   photochemical box model simulations do not confirm that increased NO causes decreased

767   CH_3OOH mixing ratios at the top of the storm core. This investigation provides guidance for

768   future studies on understanding the complex interactions between storms and chemistry for

769   peroxides. To more thoroughly understand these interactions, cloud chemistry modeling that

770   explores the various effects of entrainment, hail (especially its role in scavenging soluble trace

771   gases via the riming of cloud droplets), lightning-NO_x, and other chemistry precursors should be

772   pursued.

773

774   Previous studies estimated CH_3OOH scavenging efficiencies to be <10%, thus the high values

775   found in this study are surprising and could have implications on the chemistry downwind of

776   convection in the upper troposphere. The low CH_3OOH mixing ratios (100-350 pptv) in the

777   convective outflow observed here would produce via CH_3OOH photolysis and OH oxidation less

778   CH_2O and HO_x radicals than if less CH_3OOH were scavenged. Thus, the high scavenging

779   efficiencies of CH_3OOH may explain discrepancies between photochemical box model

780   calculations and measurements of CH_2O in convective outflow plumes, similar to those

781   described by Fried et al. [2003]. It is expected that the low H_2O_2 and CH_3OOH mixing ratios in

782   the convective outflow would have a smaller contribution to downwind O_3 production compared

783   to CH_2O, whose mixing ratios in the convective outflow ranged from 600 to 1500 pptv [Fried et

784   al., 2015]. The contribution of CH_2O and the peroxides to UT O_3 formation can be pursued

785   further via model calculations.

786

807

808

36

References

Barth, M. C., D. A. Hegg, P. V. Hobbs, J. G. Walega, G. L. Kok, B. G. Heikes, and A. L. Lazrus (1989), Measurements of atmospheric gas-phase and aqueous-phase hydrogen peroxide concentrations in winter on the east coast of the United States, Tellus, 41B, 61-69.

Barth, M. C., A. L. Stuart, and W. C. Skamarock (2001), Numerical simulations of the July 10, 1996 Stratospheric-Tropospheric Experiment: Radiation, Aerosols, and Ozone/Deep Convection Experiment storm: Redistribution of soluble tracers, J. Geophys. Res., 106, 12,381– 12,400.

Barth, M. C., P. G. Hess, and S. Madronich, (2002), Effect of marine boundary layer clouds on tropospheric chemistry as analyzed in a regional chemistry transport model, J. Geophys. Res., 107, (D11), 4126, doi:10.1029/2001JD000468.

Barth, M. C., S. Sillman, R. Hudman, M. Z. Jacobson, C.-H. Kim, A. Monod, and J. Liang (2003), Summary of the cloud chemistry modeling intercomparison: Photochemical box model simulation, J. Geophys. Res., 108(D7), 4214, doi:10.1029/2002JD002673.

Barth, M. C., S.-W. Kim, W. C. Skamarock, A. L. Stuart, K. E. Pickering, and L. E. Ott (2007a), Simulations of the redistribution of formaldehyde, formic acid, and peroxides in the 10 July 1996 Stratospheric-Tropospheric Experiment: Radiation, Aerosols, and Ozone deep convection storm, J. Geophys. Res., 112, D13310, doi:10.1029/2006JD008046.

Barth, M. C., S.-W. Kim, C. Wang, K. E. Pickering, L. E. Ott, G. Stenchikov, M. Leriche, S. Cautenet, J.-P. Pinty, Ch. Barthe, C. Mari, J. H. Helsdon, R. D. Farley, A. M. Fridlind, A. S. Ackerman, V. Spiridonov, and B. Telenta (2007b), Cloud-scale model intercomparison of chemical constituent transport in deep convection, Atmos. Chem. Phys., 7, 4709-4731, doi:10.5194/acp-7-4709-2007.

Barth, M. C., C. A. Cantrell, W. H. Brune, S. A. Rutledge, J. H. Crawford, H. Huntrieser, L. D. Carey, D. MacGorman, M. Weisman, K. E. Pickering, E. Bruning, B. Anderson, E. Apel, M. Biggerstaff, T. Campos, P. Campuzano-Jost, R. Cohen, J. Crounse, D. A. Day, G. Diskin, F. Flocke, A. Fried, C. Garland, B. Heikes, S. Honomichl, R. Hornbrook, L. G. Huey, J. Jimenez, T. Lang, M. Lichtenstern, T. Mikoviny, B. Nault, D. O'Sullivan, L. Pan, J. Peischl, I. Pollack, D. Richter, D. Riemer, T. Ryerson, H. Schlager, J. St. Clair, J. Walega, P. Weibring, A. Weinheimer, P. Wennberg, A. Wisthaler, P. Wooldridge, and C. Ziegler, (2015) The Deep Convective Clouds and Chemistry (DC3) Field Campaign, Bull. Amer. Meteor. Soc., 96, 1281–1309, doi: http://dx.doi.org/10.1175/BAMS-D-13-00290.1.

Bela, M. M., M. C. Barth, O. B. Toon, A. Fried, Y Li, K. Cummings, K. Pickering, C. Homeyer, H. Morrison, Q. Yang, D. Allen, F. Flocke, D. O'Sullivan, L. G. Huey, D. Chen, X. Lu, (2015) Wet removal of soluble species in DC3 Deep Convective storms using WRF-Chem simulations and aircraft observations, to be submitted to J. Geophys. Res.

854 Blake, N.J., B. Barletta, I. J. Simpson, J. Schroeder, S. Hughes, J. Marrero, S. Meinardi, D. R
855   Blake, E. C Apel, R. S Hornbrook, L. K Emmons (2015), Spatial distributions and source
856   characterization of trace organic gases during SEAC4RS and comparison to DC3, In
857   Preparation.
858
859 Borbon, A., et al. (2012), Transport and chemistry of formaldehyde by mesoscale convective
860   systems in West Africa during AMMA 2006, J. Geophys. Res., 117, D12301,
861
862 Brasseur A.-L., R. Ramaroson, A. Delannoy, W. Skamarock, M. Barth (2002), Three-
863   dimensional calculation of photolysis frequencies in the presence of clouds, J. Atmos. Chem.,
864   41, 211-237.
865
866 Browne, E. C., A. E. Perring, P. J. Wooldridge, E. Apel, S. R. Hall, L. G. Huey, J. Mao, K. M.
867   Spencer, J. M. St. Clair, A. J. Weinheimer, A. Wisthaler, and R. C. Cohen (2011) Global and
868   regional effects of the photochemistry of CH3O2NO2: evidence from ARCTAS, Atmos.
869   Chem. Phys., 11, 4209-4219, doi:10.5194/acp-11-4209-2011.
870
871 Chang, J. S., R. A. Brost, I. S. A. Isaksen, S. Madronich, P. Middleton, W. R. Stockwell, and C.
872   J. Walcek (1987), A three-dimensional Eulerian acid deposition model: Physical concepts
873   and formulation, J. Geophys. Res., 92(D12), 14681–14700, doi:10.1029/JD092iD12p14681.
874
875 Chin, M., P. Ginoux, S. Kinne, O. Torres, B. N. Holben, B. N. Duncan, R. V. Martin, J. A.
876   Logan, A. Higurashi, and T. Nakajima (2002), Tropospheric aerosol optical thickness from
877   the gocart model and comparisons with satellite and sun photometer measurements, Journal
878   of the Atmospheric Sciences, 59 (3), 461{483, doi:10.1175/1520-
879   0469(2002)059h0461:TAOTFTi2.0.CO;2.
880
881 Cohan, D. S., M. G. Schultz, D. J. Jacob, B. G. Heikes, and D. R. Blake (1999), Convective
882   injection and photochemical decay of peroxides in the tropical upper troposphere: Methyl
883   iodide as a tracer of marine convection, J. Geophys. Res., 104, 5717–5724.
884
885 Crum, T. D. and R. L. Alberty (1993), The WSR-88D operational support facility, Bull. Am.
886   Meteorol. Soc., 74(9), 1669-1687.
887
888 Colman, J. J., A. L. Swanson, S. Meinardi, B. C. Sive, D. R. Blake, and F. S. Rowland (2001),
889   Description of the analysis of a wide range of volatile organic compounds in whole air
890   samples collected during PEM-Tropics A and B, Anal. Chem., 73, 3723-3731.
891
892 Crutzen, P. J., and M. G. Lawrence (2000), The impact of precipitation scavenging on the
893   transport of trace gases: A 3-dimensional model sensitivity study, J. Atmos. Chem., 37, 81-
894   112.
895
896 Emmons, L. K., S. Walters, P. G. Hess, J.-F. Lamarque, G. G. Pfister, D. Fillmore, C. Granier,
897   A. Guenther, D. Kinnison, T. Laepple, J. Orlando, X. Tie, G. Tyndall, C. Wiedinmyer, S. L.
898   Baughcum, and S. Kloster (2010), Description and evaluation of the model for ozone and
899   related chemical tracers, version 4 (MOZART-4), Geoscientific Model Development, 3 (1),

38

900   43{67, doi:10.5194/gmd-3-43-2010.

902 Faloona, I. C., D. Tan, R. L. Lesher, N. L. Hazen, C. L. Frame, J. B. Simpas, H. Harder, M.
903   Martinez, P. Di Carlo, X. R. Ren, and W. H. Brune, (2004) A laser-induced fluorescence
904   instrument for detecting tropospheric OH and HO_2: Characteristics and calibration, J. Atmos.
905   Chem., 47, 139-167, doi:10.1023/B:JOCH.0000021036.53185.0e.

907 Fierro, A. O., E. R. Mansell, C. L. Ziegler, and D. R. MacGorman (2012), Application of a
908   lightning data assimilation technique in the wrf-arw model at cloud-resolving scales for the
909   tornado outbreak of 24 may 2011, Monthly Weather Review, 140 (8), 2609{2627,
910   doi:10.1175/MWR-D-11-00299.1.

912 Fried, A., et al. (2003), Airborne tunable diode laser measurements of formaldehyde during
913   TRACE-P: Distributions and box model comparisons, J. Geophys. Res., 108, 8798,
914   doi:10.1029/2003JD003451, D20.

916 Fried, A., M. C. Barth, M. M. Bela, P. Weibring, D. Richter, J. Walega, Y. Li, K. Pickering, E.
917   Apel, R. Hornbrook, A. Hills, D. D. Riemer, N. Blake, D. R. Blake, J.R. Schroeder, Z. J.
918   Luo, J. H. Crawford, J. Olson, S. Rutledge, C. R. Homeyer, G. S. Diskin, G. Sachse, T.
919   Campos, A. Weinheimer, T. Ryerson, I. Pollack, J. Peischl, K. Froyd, A. Wisthaler, T.
920   Mikoviny, and S. Woods (2015), Convective transport of formaldehyde to the upper
921   troposphere and lower stratosphere and associated scavenging in thunderstorms over the
922   central United States during the 2012 DC3 study, submitted to J. Geophys. Res.

924 Gilman, J. B., B. M. Lerner, W. C. Kuster, and J. A. de Gouw (2013), Source signature of
925   volatile organic compounds from oil and natural gas operations in Northeastern Colorado,
926   Environ. Sci. Technol., 47, 1297–1305.

928 Grell G. A., S. E. Peckham, R. Schmitz, S. A. McKeen, G. Frost, W. C. Skamarock, and B. Eder
929   (2005), Fully coupled 'online' chemistry in the WRF model, Atmos. Environ., 39, 6957-6976.

931 Guenther, A., T. Karl, P. Harley, C. Wiedinmyer, P. I. Palmer, and C. Geron (2006), Estimates of
932   global terrestrial isoprene emissions using MEGAN (Model of Emissions of Gases and
933   Aerosols from Nature), Atmospheric Chemistry and Physics, 6 (11), 3181{3210,
934   doi:10.5194/acp-6-3181-2006.

936 Homeyer, C. R. (2014), Formation of the enhanced-v infrared cloud-top feature from high-
937   resolution three-dimensional radar observations. J. Atmos. Sci., 71, 332–348. doi:
938   http://dx.doi.org/10.1175/JAS-D-13-079.1

940 Homeyer, C. R. and M. R. Kumjian (2015), Microphysical characteristics of overshooting
941   convection from polarimetric radar observations. J. Atmos. Sci., 72, 870–891. doi:
942   http://dx.doi.org/10.1175/JAS-D-13-0388.1

944 Hong, S.-Y., Y. Noh, and J. Dudhia (2006), A new vertical diffusion package with an explicit
945   treatment of entrainment processes, Monthly Weather Review, 134 (9), 2318-2341,

946   doi:10.1175/MWR3199.1.
947

948 Huntrieser, H., M. Lichtenstern, M. Scheibe, H. Aufmhoff, H. Schlager, T. Pucik, A. Minikin1,
949   B. Weinzierl, K. Heimerl, I. B. Pollack, J. Peischl, T. B. Ryerson, A. J. Weinheimer, S.
950   Honomichl, B. A. Ridley, M. I. Biggerstaff, D. P. Betten, J. W. Hair, C. F. Butler, M. J.
951   Schwartz, and M. C. Barth (2015a) Injection of lightning-produced NO_x, water vapor,
952   wildfire emissions, and stratospheric air to the UT/LS as observed from DC3
953   measurements, submitted to J. Geophys. Res.
954

955 Huntrieser, H., M. Lichtenstern, M. Scheibe, H. Aufmhoff, H. Schlager, T. Pucik, A. Minikin1,
956   B. Weinzierl, K. Heimerl, D. Fütterer, B. Rappenglück, L. Ackermann, K. E. Pickering, K.
957   A. Cummings, M. I. Biggerstaff, D. P. Betten, S. Honomichl, and M. C. Barth (2015b), On
958   the origin of pronounced O_3 gradients in the thunderstorm outflow region during DC3,
959   submitted to J. Geophys. Res.
960

961 Iacono, M. J., J. S. Delamere, E. J. Mlawer, M. W. Shephard, S. A. Clough, and W. D. Collins
962   (2008), Radiative forcing by long-lived greenhouse gases: Calculations with the AER
963   radiative transfer models, J. Geophys. Res., 113, D13103, doi:10.1029/2008JD009944.
964

965 Jaeglé, L., et al. (1997) Observed OH and HO_2 in the upper troposphere suggest a major source
966   from convective injection of peroxides, Geophys. Res. Lett., 24, 3181-3184.
967

968 Kim, S., et al. (2007), Measurement of HO2NO2 in the free troposphere during the
969   Intercontinental Chemical Transport Experiment–North America 2004, J. Geophys. Res.,
970   112, D12S01, doi:10.1029/2006JD007676.
971

972 Kim, S.-W., M. C. Barth, and M. Trainer (2012), Influence of fair-weather clouds on isoprene
973   chemistry, J. Geophys. Res., 117, D10302, doi:10.1029/2011JD017099.
974

975 Lawson, R. P., D. O'Connor, P, Zmarzly, K. Weaver, B. Baker, and Q. Mo (2006), The 2D-S
976   (Stereo) Probe: Design and Preliminary Tests of a New Airborne, High-Speed, High-
977   Resolution Particle Imaging Probe, J. Atmos. Ocean. Tech., 23, 1462-1477.
978

979 Lee, S. S., L. J. Donner, V. T. J. Phillips, and Y. Ming (2008), The dependence of aerosol effects
980   on clouds and precipitation on cloud-system organization, shear and stability, J. Geophys.
981   Res., 113, D16202, doi:10.1029/2007JD009224.
982

983 Leriche, M. Pinty, J.-P., Mari, C., and Gazen, D. (2013), A cloud chemistry module for the 3-D
984   cloud-resolving mesoscale model Meso-NH with application to idealized cases, Geosci.
985   Model Dev., 6, 1275-1298, doi:10.5194/gmd-6-1275-2013.
986

987 Luo, Z. J., G. Y. Liu, and G. L. Stephens (2010), Use of A-Train data to estimate convective
988   buoyancy and entrainment rate, Geophys. Res. Lett., 37, L09804,
989   doi:10.1029/2010GL042904.
990

40

991   Macdonald, A. M., K. G. Anlauf, C. M. Banic, W. R. Leaitch, and H. A. Wiebe (1995), Airborne
992   measurements of aqueous and gaseous hydrogen peroxide during spring and summer in
993   Ontario, Canada, J. Geophys. Res., 100(D4), 7253–7262, doi:10.1029/95JD00194.
994
995   Morrison, H., G. Thompson, and V. Tatarskii (2009), Impact of cloud microphysics on the
996   development of trailing stratiform precipitation in a simulated squall line: Comparison of
997   one- and two-moment schemes, Mon. Weather Review, 137 (3), 991{1007,
998   doi:10.1175/2008MWR2556.1.
999
1000 Nault, B. A., C. Garland, S. E. Pusede, P. J. Wooldridge, K. Ullmann, S. R. Hall, and R. C.
1001   Cohen, (2015) Measurements of $CH_3O_2NO_2$ in the upper troposphere, Atmos. Meas. Tech.,
1002   8, 987-997, doi:10.5194/amt-8-987-2015.
1003
1004 Neu, J. L. and Prather, M. J. (2012) Toward a more physical representation of precipitation
1005   scavenging in global chemistry models: cloud overlap and ice physics and their impact on
1006   tropospheric ozone, Atmos. Chem. Phys., 12, 3289-3310, doi:10.5194/acp-12-3289-2012.
1007
1008 Nguyen, T. B., Crounse, J. D., Teng, A. P., St. Clair, J. M., Paulot, F., Wolfe, G. M., and
1009   Wennberg, P. O. (2015) Rapid Deposition of Oxidized Biogenic Compounds to a Temperate
1010   Forest Proc. Natl. Acad. Sci., 112, E392– E401, doi:10.1073/pnas.1418702112.
1011
1012 Paulot, F., J. D. Crounse, H. G. Kjaergaard, A. Kurten, J. M. St. Clair, J. H. Seinfeld, and P. O.
1013   Wennberg (2009), Unexpected epoxide formation in the gas-phase photooxidation of
1014   isoprene, Science, 325 (5941), 730-733.
1015
1016 Pollack, I. B., B. M. Lerner, and T. B. Ryerson (2011), Evaluation of ultraviolet light-emitting
1017   diodes for detection of atmospheric NO_2 by photolysis - chemiluminescence, J. Atmos.
1018   Chem., 65(2), 111-125, doi:10.1007/s10874-011-9184-3.
1019
1020 Prather, M. J., and D. J. Jacob, (1997) A, persistent imbalance in HOx and NOx photochemistry
1021   of the upper troposphere driven by deep tropical convection, Geophys Res. Lett., 24, 3189-
1022   3192.
1023
1024 Ravetta, F., D. J. Jacob, W. H. Brune, D. Tan, I.F. Faloona, B. G. Heikes, B. Anderson, D. R.
1025   Blake, G. L. Gregory, G. W. Sachse, S. T. Sandholm, R. E. Shetter, H. B. Singh, and R. W.
1026   Talbot, (2001) Experimental evidence for the importance of convected methylhydroperoxide
1027   as a source of hydrogen oxide (HOx) radicals in the tropical upper troposphere. J. Geophys.
1028   Res., 106, 32,709-32,716, doi:10.1029/2001JD900009.
1029
1030 Sander, R. (2015), Compilation of Henry's law constants (version 4.0) for water as solvent,
1031   Atmos. Chem. Phys., 15, 4399-4981, doi:10.5194/acp-15-4399-2015.
1032
1033 Sander, S. P., J. Abbatt, J. R. Barker, J. B. Burkholder, R. R. Friedl, D. M. Golden, R. E. Huie,
1034   C. E. Kolb, M. J. Kurylo, G. K. Moortgat, V. L. Orkin and P. H. Wine (2011), "Chemical
1035   Kinetics and Photochemical Data for Use in Atmospheric Studies, Evaluation No. 17," JPL
1036   Publication 10-6, Jet Propulsion Laboratory, Pasadena, http://jpldataeval.jpl.nasa.gov.

1037

1038 Scala, J. R., et al. (1990), Cloud draft structure and trace gas transport, J. Geophys. Res.,
1039   95(D10), 17,015–17,030, doi:10.1029/JD095iD10p17015.

1040

1041 Schroeder, J. R., L. L. Pan, T. Ryerson, G. Diskin, J. Hair, S. Meinardi, I. Simpson, B. Barletta,
1042   N. Blake, and D. R. Blake (2014), Evidence of mixing between polluted convective outflow
1043   and stratospheric air in the upper troposphere during DC3, J. Geophys. Res. Atmos., 119,
1044   11,477–11,491, doi:10.1002/2014JD022109.

1045

1046 Seinfeld, J. and S. Pandis (1998) Atmospheric Chemistry and Physics: From Air Pollution to
1047   Climate Change, Wiley, New York, USA.

1048

1049 Simpson, I. J., N. J. Blake, B. Barletta, G. S. Diskin, H. E. Fuelberg, K. Gorham, L. G. Huey, S.
1050   Meinardi, F. S. Rowland, S. A. Vay, A. J. Weinheimer, M. Yang, and D. R. Blake (2010),
1051   Characterization of trace gases measured over Alberta oil sands mining operations: 76
1052   speciated C2–C10 volatile organic compounds (VOCs), CO2, CH4, CO, NO, NO2, NOy, O3
1053   and SO2, Atmos. Chem. Phys., 10, 11931-11954, doi:10.5194/acp-10-11931-2010.

1054

1055 Snow, J. A., B. G. Heikes, H. Shen, D. W. O'Sullivan, A. Fried, and J. Walega (2007), Hydrogen
1056   peroxide, methyl hydroperoxide, and formaldehyde over North America and the North
1057   Atlantic, J. Geophys. Res., 112, D12S07, doi:10.1029/2006JD007746.

1058

1059 St. Clair, J. M., D. C. McCabe, J. D. Crounse, U. Steiner, and P. O. Wennberg (2010), Chemical
1060   ionization tandem mass spectrometer for the in situ measurement of methyl hydrogen
1061   peroxide, Rev. Sci. Instrum., 81 (9), 094102, doi: 10.1063/1.3480552.

1062

1063 Stuart, A. L., and M. Z. Jacobson (2006), A numerical model of the partitioning of trace
1064   chemical solutes during drop freezing, J. Atmos. Chem., 53, 13– 42.

1065

1066 Swarthout, R. F.; Russo, R. S.; Zhou, Y.; Hart, A. H.; Sive, B. C. (2013) Volatile organic
1067   compound distributions during the NACHTT campaign at the Boulder Atmospheric
1068   Observatory: Influence of urban and natural gas sources. J. Geophys. Res.: Atmos., 118 (18),
1069   10614−10637.

1070

1071 Taylor, J. R. (1982) An introduction to error analysis: the study of uncertainties in physical
1072   measurements, University Science Books, Mill Valley, California, USA.

1073

1074 Thompson, A. M., K. E. Pickering, R. R. Dickerson, W. G. Ellis Jr., D. J. Jacob, J. R. Scala, W.-
1075   K. Tao, D. P. McNamara, and J. Simpson (1994), Convective transport over the central
1076   United States and its role in regional CO and ozone budgets, J. Geophys. Res., 99(D9),
1077   18,703–18,711, doi:10.1029/94JD01244.

1078

1079 Thornton, J. A., P. J. Wooldridge, and R. C. Cohen (2000), Atmospheric NO_2: In situ laser-
1080   induced fluorescence detection at parts per trillion mixing ratios, Anal. Chem. 72, 528–539.

1081

1082   Wang, C. (2005), A modeling study of the response of tropical deep convection to the increase of
1083   cloud condensation nuclei concentration: 2. Radiation and tropospheric chemistry, J.
1084   Geophys. Res., 110, D22204, doi:10.1029/2005JD005829.
1085

1086   Weisman, M. L. and J. B. Klemp (1982), The dependence of numerically simulated convective
1087   storms on vertical wind shear and buoyancy. Mon. Wea. Rev., 110, 504–520. doi:
1088   http://dx.doi.org/10.1175/1520-0493(1982)110<0504:TDONSC>2.0.CO;2
1089

1090   Weisman, M. L., J. B. Klemp, and R. Rotunno, (1988), Structure and Evolution of Numerically
1091   Simulated Squall Lines. J. Atmos. Sci., 45, 1990–2013, doi: http://dx.doi.org/10.1175/1520-
1092   0469(1988)045<1990:SAEONS>2.0.CO;2
1093

1094   Wennberg, P. O., et al. (1998), Hydrogen radicals, nitrogen radicals, and the production of O_3 in
1095   the upper troposphere, Science, 279, 49– 53.
1096

1097   Wesely, M. (1989), Parameterization of surface resistances to gaseous dry deposition in regional-
1098   scale numerical models, Atmos. Environ., 23, 1293–1304.
1099

1100   Wiedinmyer, C., S. K. Akagi, R. J. Yokelson, L. K. Emmons, J. A. Al-Saadi, J. J. Orlando, and
1101   A. J. Soja (2011), The fire inventory from NCAR (FINN): A high resolution global model to
1102   estimate the emissions from open burning, Geosci. Model Dev., 4 (3), 625{641,
1103   doi:10.5194/gmd-4-625-2011.
1104

1105   Yang, Q., R. C. Easter, P. Campuzano-Jost, J. L. Jimenez, J. D. Fast, S. J. Ghan, H. Wang, L. K.
1106   Berg, M. C. Barth, Y. Liu, et al. (2015), Aerosol transport and wet scavenging in deep
1107   convective clouds: A case study and model evaluation using a multiple passive tracer
1108   analysis approach, J. Geophys. Res., 120, doi:10.1002/2015JD023647.
1109
1110
1111
1112

1113 **Tables**

1114

1115

1116 **Table 1.** List of data and instruments used in the analysis.

Species/Parameter	Instrument[a]	Uncertainty
H_2O_2, CH_3OOH	CIT-CIMS	H_2O_2 (pptv): $75 + 0.5$ [H_2O_2] CH_3OOH (pptv): $30 + 0.4$[CH_3OOH] at H_2O vapor < 230 ppmv $30 + (-9.1 + log_{10}$[H_2O]) [CH_3OOH] at H_2O vapor > 230 ppmv
n-butane, i-butane, n-pentane, i-pentane	WAS	5% or 3 pptv
NO, NO_2 [b]	CSD CL	NO (pptv): $10 + 0.04$ [NO] NO_2 (pptv): $20 + 0.06$ [NO_2]
NO_2, MPN[c]	TD-LIF	NO_2: 5% MPN: 40%
OH, HO_2	ATHOS	32%
SO_2	GT-CIMS	15%
H_2O vapor	DLH	5% or 1 ppmv
Pressure, Temperature, 3D Winds	MMS	Pressure: 0.5% Temperature: 0.2% Winds: 3%
Ice water content	2DS	Not available

1117 [a]CIT-CIMS is California Institute of Technology chemical ionization mass spectrometry; WAS is the
1118 Whole Air Sampler that uses gas chromatography; CSD CL is NOAA Chemical Science Division
1119 chemiluminescence; TD-LIF is thermal dissociation – laser induced fluorescence; ATHOS is Airborne
1120 Tropospheric Hydrogen Oxides Sensor that uses laser induced fluorescence; GT-CIMS is Georgia
1121 Institute of Technology chemical ionization mass spectrometry; DLH is diode laser hygrometer that uses
1122 differential absorption spectroscopy; MMS is Meteorological Measurement System; 2DS is two-
1123 dimensional stereo probe.
1124 [b]The NO_2 measurement should be interpreted as the sum of NO_2 and MPN based on the findings of
1125 Browne et al. [2011].
1126 [c]MPN is methyl peroxy nitrate.

1127

1128

1129

44

1130
1131 **Table 2.** DC3 cases investigated.

Date	Location	CAPE (J kg^{-1})	0-6 km Vertical Wind Shear (m s^{-1})	Cloud base to Freezing Level Depth (m)	Freezing Level to -40°C Depth (m)
18 May 2012	Southwest Nebraska	1144	12.1	121	4910
29 May 2012	Northern Oklahoma	3113	19.0	2505	5780
02 June 2012	Northeast Colorado	918	13.2	640	5172
06 June 2012	Northeast Colorado	2981	17.5	1157	5145
16 June 2012	Central Oklahoma	3049	15.9	2762	5803
22 June 2012	Southwest Nebraska	2563	24.2	1750	5229

Table 3. Inflow and outflow times (UTC) and altitude (km, MSL) of measurements from the DC-8 aircraft used for analysis.

Date	Inflow Time (UTC)	Inflow Altitude (km)	Outflow Time (UTC)	Outflow Altitude (km)
18 May 2012	22:48:29-22:51:10	1.7	23:17:50-23:22:00	11.3
29 May 2012	23:10:21-23:15:53	1.3	23:49:18-23:58:13	11.0
02 June 2012	21:16:18-21:27:38	1.9	22:40:46-22:46:10	11.1
06 June 2012	22:13:40-22:25:12	1.7	23:57:22-24:01:59	12.4
16 June 2012	24:15:00-24:20:00	0.95	25:50:00-25:55:00	11.9
22 June 2012	22:31:27-22:45:54	2.0	25:16:51-25:19:24	11.2

Table 4. Configuration of the WRF simulation.

Process	Parameterization	Reference
Meteorology Initialization	North American Mesoscale Analysis with pre-storm lightning data assimilation	Fierro et al. [2012]
Cloud microphysics	Morrison 2-moment	Morrison et al. [2009]
Deep/shallow convection	none	
Planetary boundary layer	YSU[a]	Hong et al. [2006]
Land surface	Noah	
Short/longwave radiation	RRTMG[b]	Iacono et al. [2008]
Chemistry Initialization	Combination of aircraft measurements and MOZART global chemistry transport model	Bela et al. [2015] Emmons et al. [2010]
Anthropogenic Emissions	EPA NEI 2011	
Biogenic Emissions	MEGAN[c] v2.04	Guenther et al. [2006]
Biomass Burning Emissions	FINN[d]	Wiedinmyer et al. [2011]
Gas-phase Chemistry Mechanism	MOZART[e]	Emmons et al. [2010]
Aerosol Physics and Chemistry	GOCART[f]	Chin et al. [2002]
Dry Deposition	Resistance method	Wesely [1989]
Wet Deposition	Henry's Law equilibrium with net production of precipitation	Neu and Prather [2012]

[a]YSU = Yonsei University scheme; [b]RRTMG = Rapid Radiative Transfer Model for GCMs; [c]MEGAN = Model of Emissions of Gases and Aerosols from Nature; [d]FINN = Fire Inventory from NCAR; [e]MOZART = Model for Ozone and Related Chemical Tracers; [f]GOCART = Goddard Chemistry Aerosol Radiation and Transport model.

Table 5. Percent contributions of each 1-km altitude layer to the storm core top as determined from the WRF-Chem simulation.

Layer Bottom Altitude (km)	Layer Top Altitude (km)	Percent Contribution (%)
0	1	6.4 ± 4.8
1	2	12. ± 7.8
2	3	9.4 ± 5.5
3	4	5.0 ± 3.1
4	5	5.8 ± 3.6
5	6	8.5 ± 5.7
6	7	9.4 ± 6.7
7	8	8.4 ± 5.9
8	9	8.3 ± 7.9
9	10	5.7 ± 12.
10	11	0.26 ± 0.86
11	12	0.01 ± 0.02
Average for 1-11 km altitudes		7.3 ± 3.3

Table 6. Mixing ratios of H_2O_2 (pptv) and CH_3OOH (pptv) averaged for the inflow and outflow times. The uncertainties of the average values are included.

Date	Inflow Time		Outflow Time	
	H_2O_2	CH_3OOH	H_2O_2	CH_3OOH
18 May 2012	665±407	571±453	87±119	102±71
29 May 2012	2462±1306	1522±1276	169±160	175±104
02 June 2012	2108±1129	580±459	60±105	199±109
06 June 2012	4135±2142	1148±911	94±122	126±81
16 June 2012	1777±964	1655±1381	90±120	336±164
22 June 2012	1544±847	647±499	255±203	276±145

Table 7. Mixing ratios of n-butane, i-butane, n-pentane, i-pentane (pptv) and the i-butane/n-butane and i-pentane/n-pentane ratios averaged for the inflow and outflow regions. The standard deviations of the averages are included.

Date	Inflow Region		Outflow Region		Inflow	Outflow
	n-butane	**i-butane**	**n-butane**	**i-butane**	**i-butane/n-butane**	
18 May 2012	1511±45	537±16	431±65	164±23	0.36	0.38
29 May 2012	1548±31	513±10	763±61	280±25	0.33	0.37
02 June 2012	262±68	112±25	108±3	51±3	0.43	0.48
06 June 2012	312±28	132±10	224±2[a]	95±4[a]	0.42	0.39
16 June 2012	1746±514	678±165	406±39	169±19	0.40	0.42
22 June 2012	194±25	70±11	150±3	52±3	0.36	0.35
	n-pentane	**i-pentane**	**n-pentane**	**i-pentane**	**i-pentane/n-pentane**	
18 May 2012	365±11	377±11	107±17	110±18	1.03	1.03
29 May 2012	457±9	397±8	202±17	210±26	0.87	1.04
02 June 2012	68±19	72±25	31±3	32±3	1.05	1.02
06 June 2012	80±8	84±13	56±1[a]	54±1[a]	1.05	0.96
16 June 2012	596±202	550±145	105±21	109±18	0.92	1.04
22 June 2012	44±4	49±5	42±3	34±3	1.11	0.81

[a]Values from Fried et al. [2015] using the outflow measurements from both the DC-8 and GV. These values are extrapolated to the top of the storm core as described by Fried et al. [2015].

Table 8. Entrainment rate and scavenging efficiencies for each storm analyzed.

Date	Entrainment Rate (% km^{-1})	Scavenging Efficiencies (%)	
		H_2O_2	CH_3OOH
18 May 2012	14.1 ± 0.3	84 ± 23	58 ± 35
29 May 2012	7.6 ± 1.6	88 ± 11	77 ± 20
02 June 2012	16.5 ± 4.6	94 ± 13	12 ± 67
06 June 2012	4.1[*] ± 0.7	97 ± 05	84 ± 15
16 June 2012	17.2 ± 1.7	89 ± 15	30 ± 50
22 June 2012	4.8 ± 0.9	79 ± 19	44 ± 47

[*]Entrainment rate is from Fried et al. [2015].
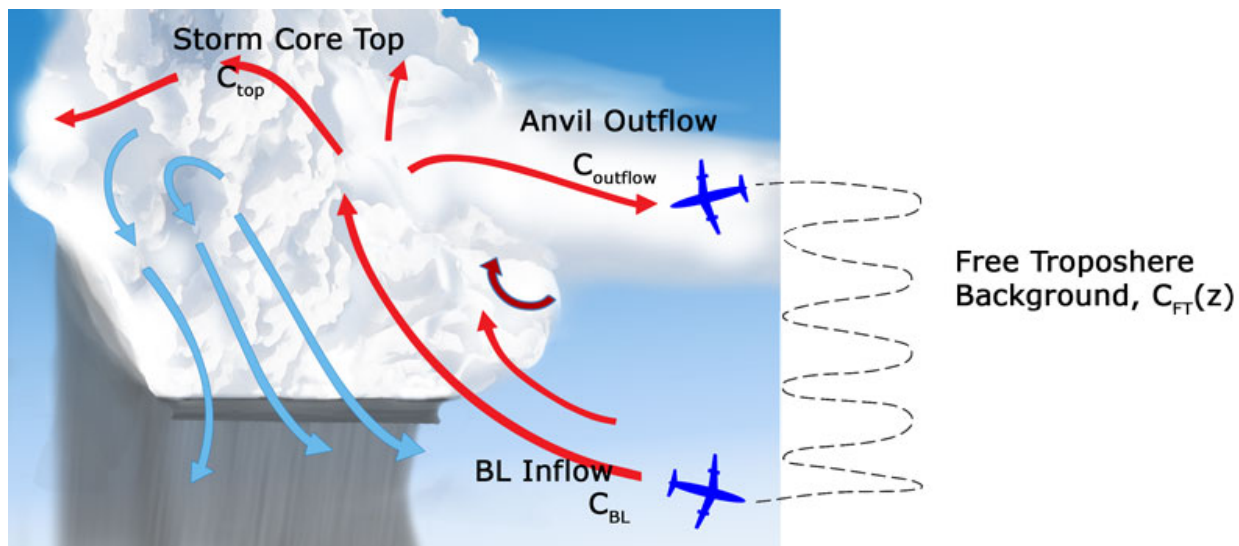
Figures

Figure 1. Air motions associated with deep convection in an environment with high vertical wind shear. The schematic is annotated with locations of the measured trace gas mixing ratios in the boundary layer inflow, free troposphere background, anvil outflow, and storm core top. Also shown is a schematic of the DC-8 flight pattern for sampling clear air profiles near the thunderstorm.
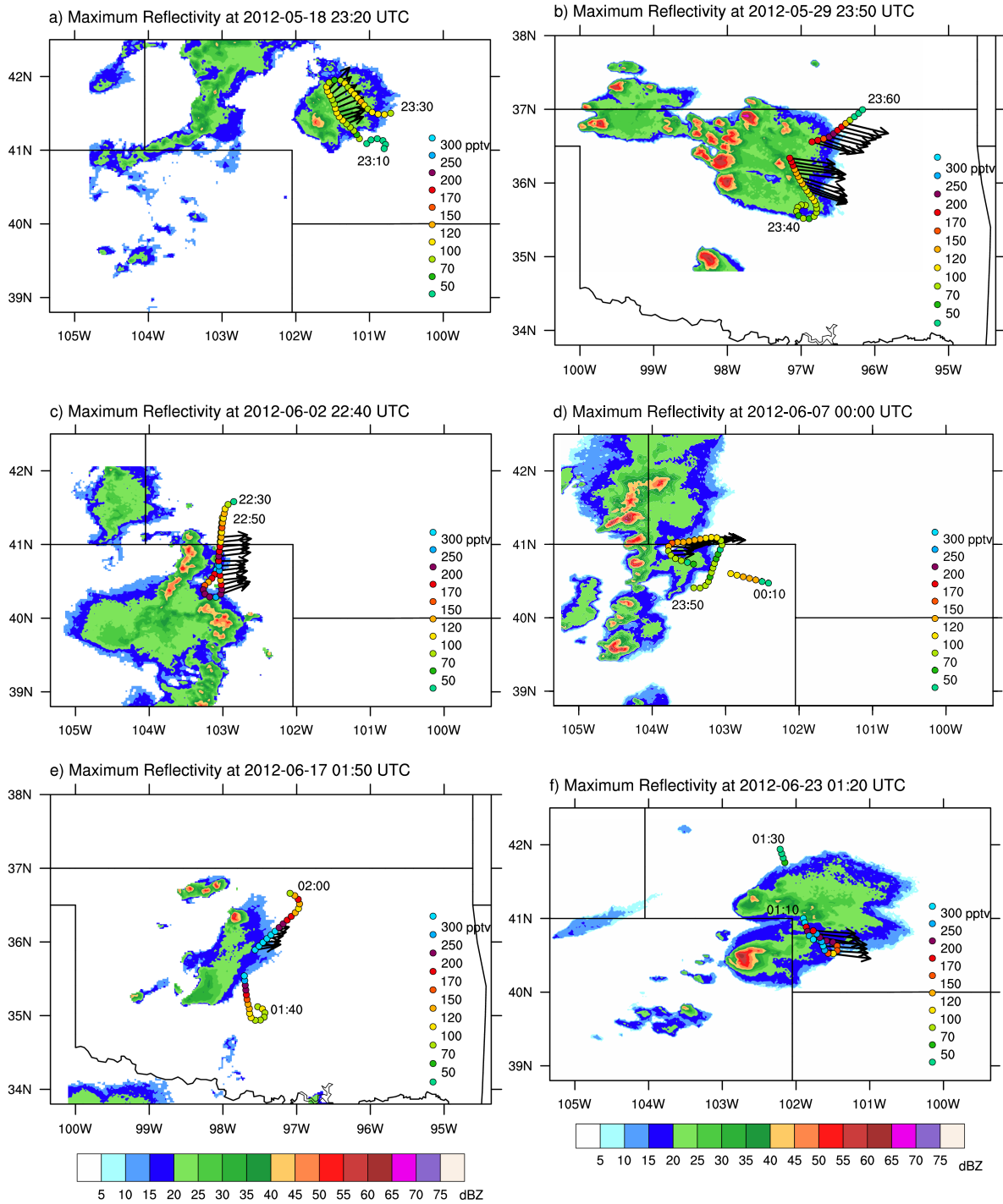
Figure 2. Maximum column reflectivity from the NWS NEXRAD radars for a) 18 May southwest Nebraska, b) 29 May Oklahoma, c) 2 June Colorado, d) 6 June Colorado, e) 16 June Oklahoma, and f) 22 June Colorado DC3 cases. Overlaid is the NASA DC-8 aircraft flight track with the start and end times of the outflow flight leg and colored by the mixing ratio of CH₃OOH (pptv) for the 20 minutes surrounding the time of the radar reflectivity image. Vectors indicate the aircraft winds for times when outflow data were used for the scavenging efficiency calculation.

51
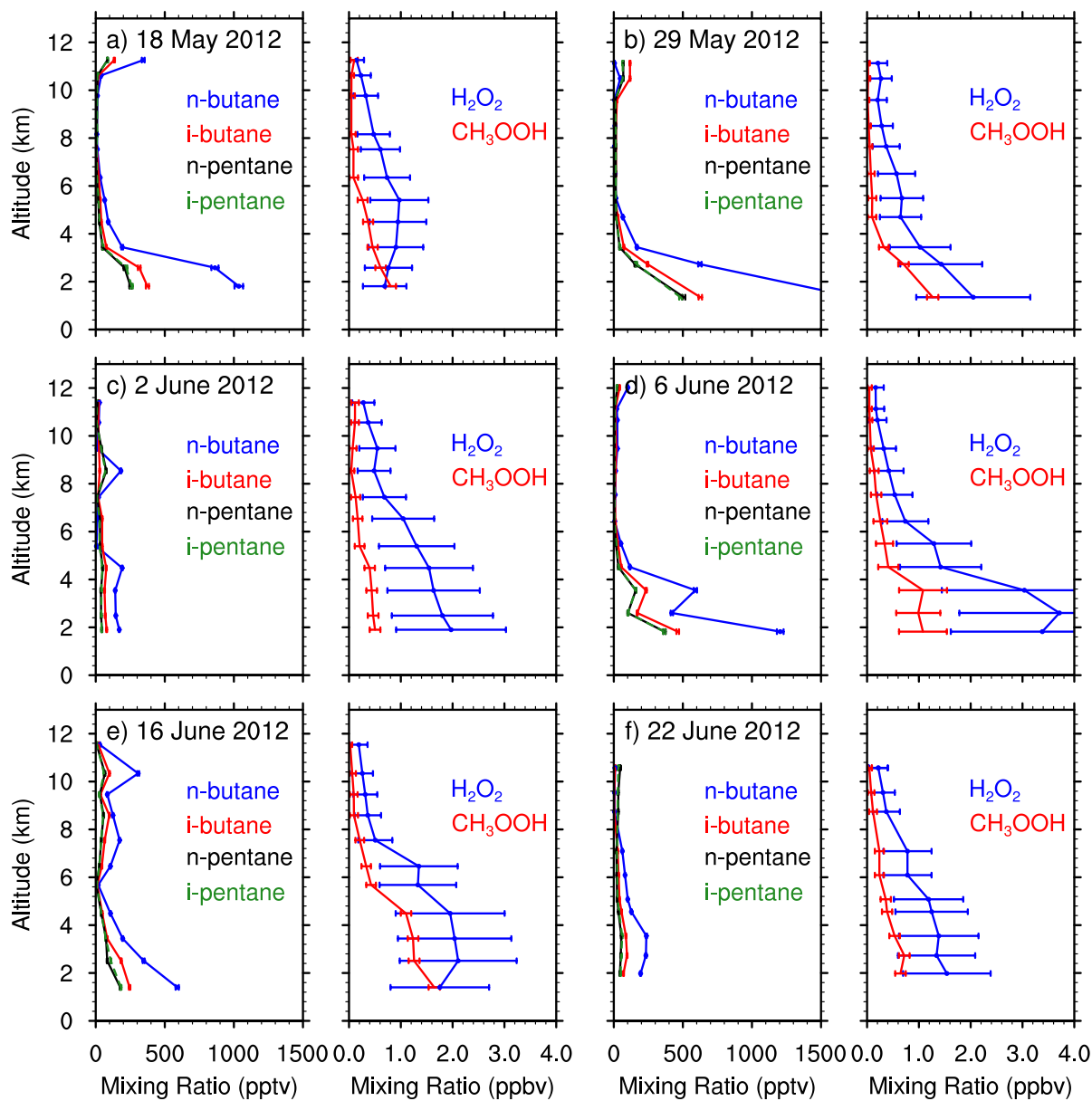
Figure 3. Cloud-free vertical profiles of n-butane (blue), i-butane (red), n-pentane (black), i-pentane (green), and H_2O_2 (blue) and CH_3OOH (red) for the a) 18 May, b) 29 May, c) 2 June, d) 6 June, e) 16 June, and 22 June 2012 DC3 cases.
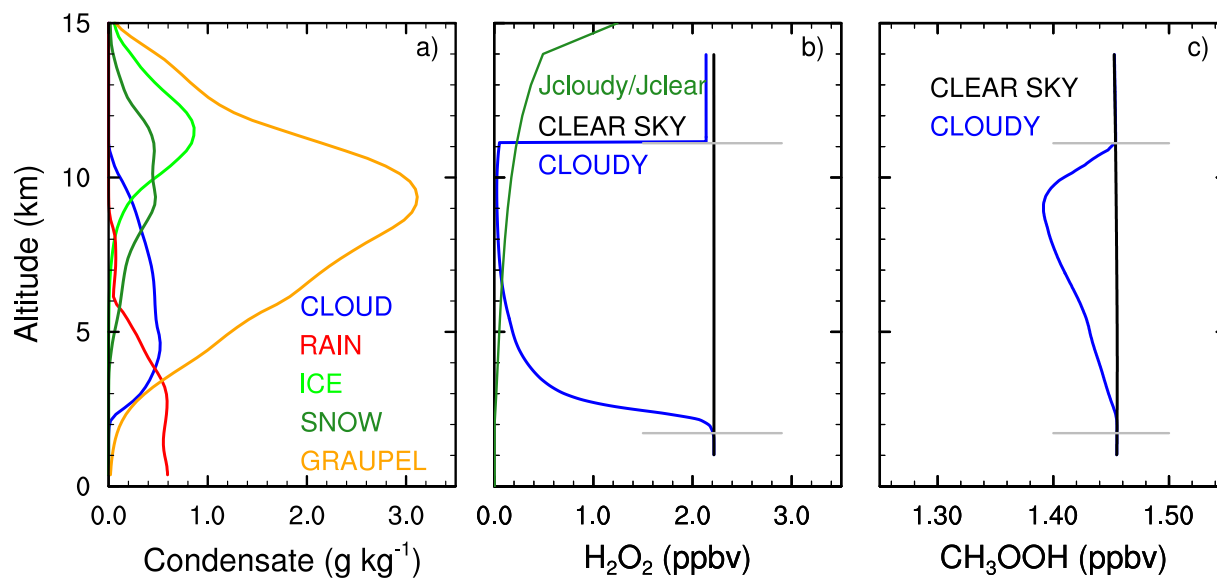
Figure 4. Vertical profiles of a) storm hydrometeor mixing ratios obtained from the WRF-Chem simulation, and gas-phase b) H_2O_2 and c) CH_3OOH mixing ratios calculated by the gas-aqueous photochemical box model. In panel a), cloud water is the blue line, rain the red line, ice the green line, snow the dark green line, and graupel/hail the orange line. In panels b) and c), the gas chemistry only simulation is the black line, and the gas-aqueous chemistry is the blue line and used the cloud water mixing ratios shown in a). The cloud water base and top are marked by the horizontal gray lines. In b) the ratio of the cloudy to clear sky H_2O_2 photolysis rate at 00 UTC is shown in dark green.
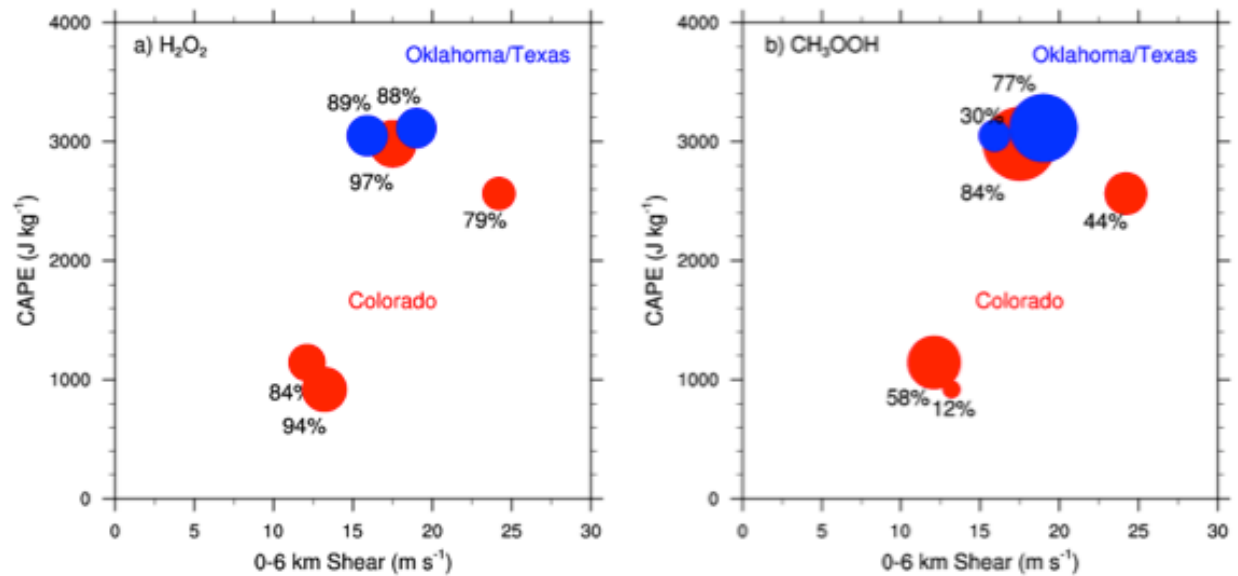
Figure 5. Scavenging efficiencies of H_2O_2 (a) and CH_3OOH (b) placed in the CAPE – low-level vertical wind shear parameter space. The size of the circles is scaled to the scavenging efficiency values. Blue circles denote Oklahoma storms and red circles are Colorado storms.
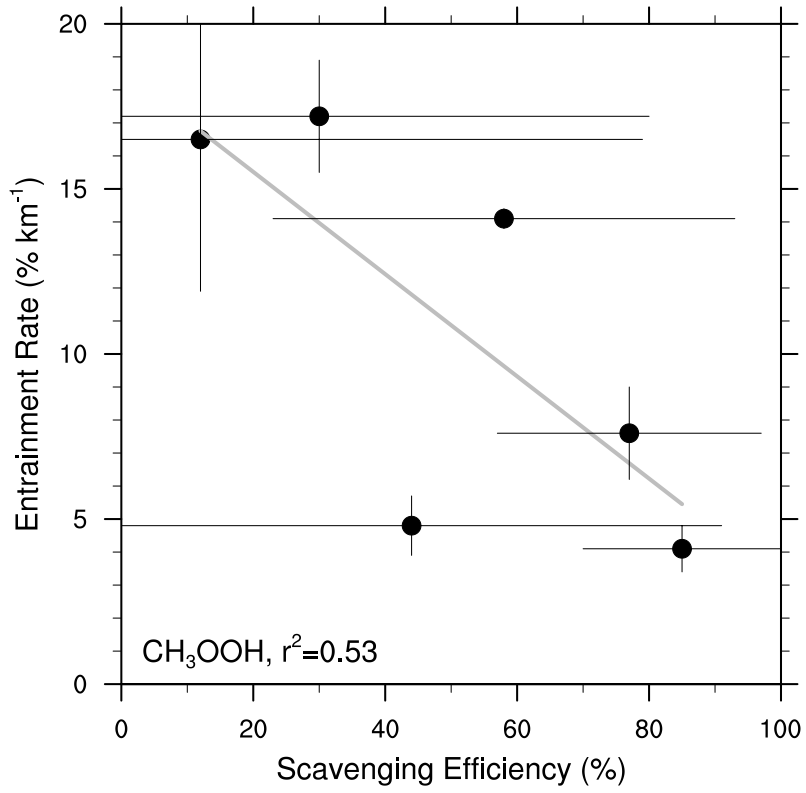
54

Figure 6. Correspondence of estimated CH_3OOH scavenging efficiencies and storm entrainment rates. The gray line in each plot represents the regression line for the data shown.
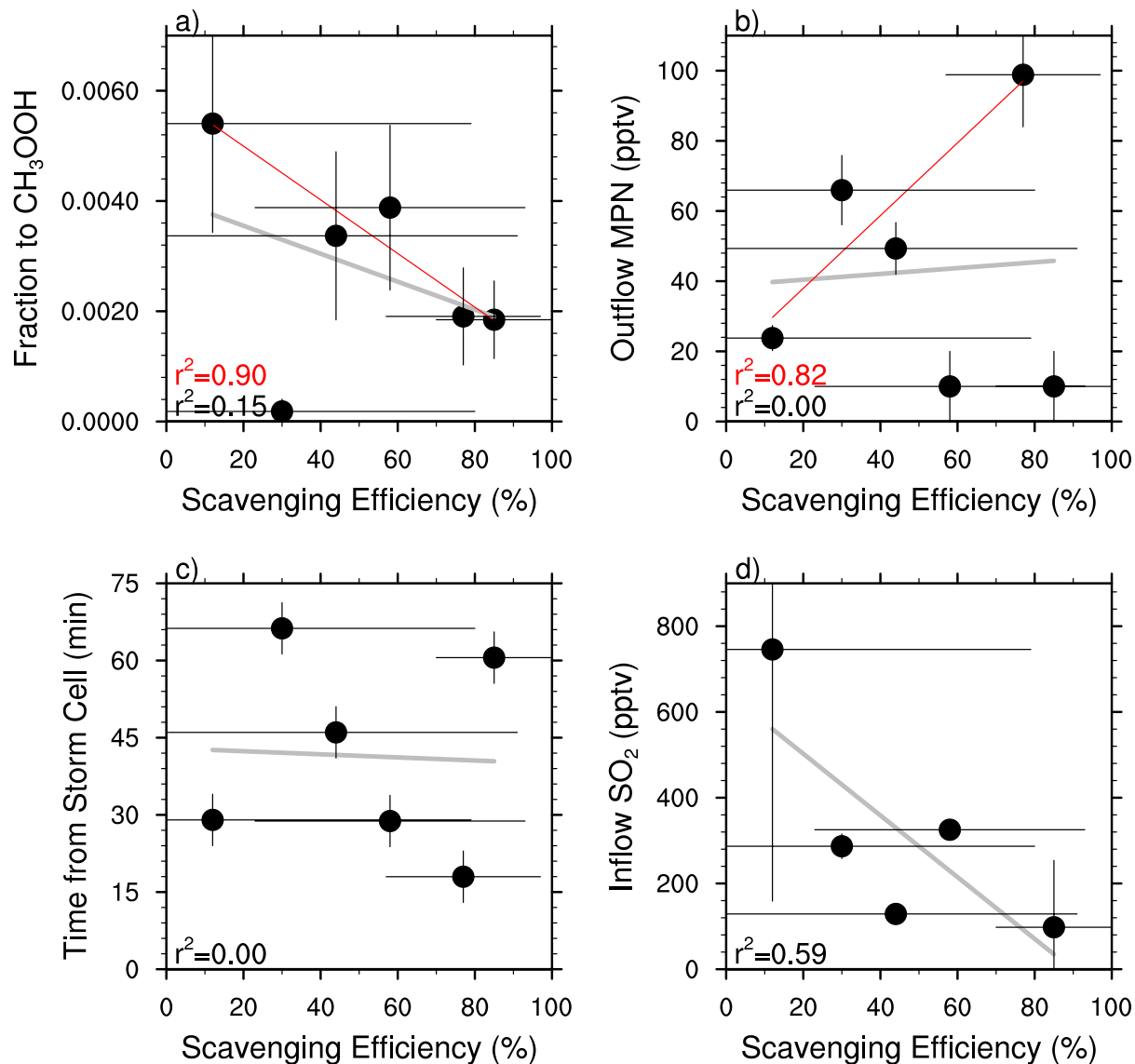
Figure 7. Correspondence of CH₃OOH scavenging efficiency with estimated a) fraction of CH_3OO producing CH_3OOH, b) 60-s averaged methyl peroxy nitrate data in the outflow flight leg, c) time traveled by sampled air from storm cell to the aircraft in the outflow region, and d) average SO_2 mixing ratio in the inflow region of the storm. See text for details on how each parameter was estimated. The gray line in each plot represents the regression line for the data shown. The red line in panels a) and b) represents the regression line for the data without the 16 June data point and without the 18 May and 6 June data points, respectively.
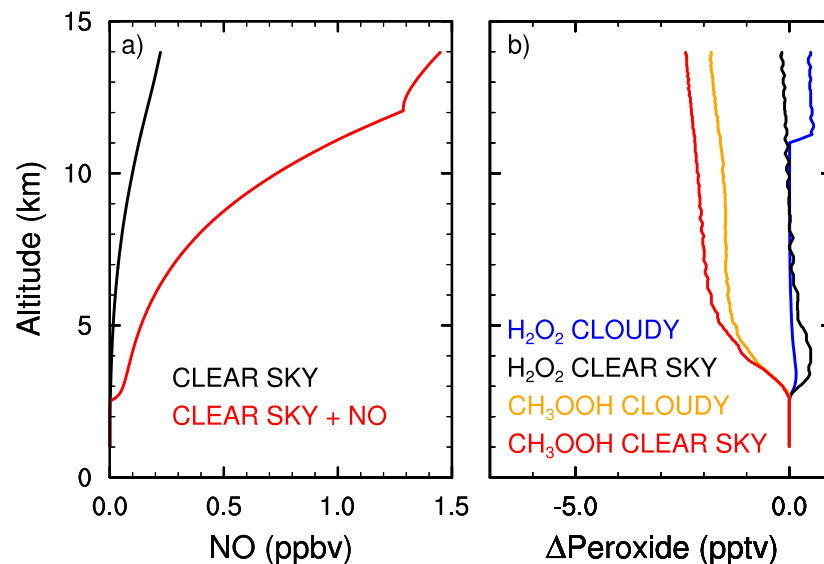
Figure 8. Vertical profiles of gas-phase a) NO calculated by the photochemical gas-aqueous chemistry box model, and b) the difference between gas-phase H_2O_2 and CH_3OOH mixing ratios between the simulations with and without the NO source. The black and blue lines are H_2O_2 differences from the gas-only chemistry and gas-aqueous chemistry simulations, respectively. The red and orange lines are CH_3OOH differences from the gas-only and gas-aqueous chemistry simulations, respectively.